DNA replication fork speed Acts as an Engine in Cortical Neurogenesis

Jianhong Wang[1,2,3], Yifan Kong[1,2,3], Xuezhuang Li[1,4], Yulian Tan[1,2], Kun Xiang[5], Juan Carlos Izpisua Belmonte[6*], Lei Shi[1,2,7*]

[1]Key Laboratory of Genetic Evolution & Animal Models, Kunming Institute of Zoology, Chinese Academy of Sciences, Kunming, 650201, P.R. China

[2]Key Laboratory of Animal Models and Human Disease Mechanisms of Yunnan Province, Kunming Institute of Zoology, Chinese Academy of Sciences, Kunming, Yunnan 650223, P.R. China

[3]Kunming College of Life Science, University of Chinese Academy of Sciences, Kunming, Yunnan, 650201, P.R. China

[4]School of Life Sciences, Zhengzhou University, Zhengzhou, Henan, 450001, P.R. China.

[5]The First People's Hospital of Yunnan Province, Kunming, Yunnan, 650034, P.R. China

[6]Altos Labs, 5510 Morehouse Drive, Suite 300, San Diego, CA 92121, USA

[7]Lead Contact

*Correspondence should be addressed to:

J.C.I.B. jcbelmonte@altoslabs.com

L.S. shilei@mail.kiz.ac.cn

SUMMARY

DNA fork speed, the rate of replication fork progression, has emerged as a cellular plasticity regulator, however, for its role in neurogenesis has never been explored before. Here, we show that fork speed was increased as neural progenitors-radial glial cells (RGCs) transition from symmetric to asymmetric divisions. After selectively deleting mini-chromosome maintenance complex (MCMs)-binding protein (MCMBP), fork speed was increased in RGCs, resulted in widespread apoptosis, DNA damage and micronuclei at later stage of neurogenesis, which triggered p53 activation and led to microcephaly. Further, co-deletion of *Trp53* with *Mcmbp* largely rescued brain phenotype, however, fork speed became faster, unexpectedly resulting in massive RGCs detachment from their resident place. Mechanistically, MCM3 can interact with p53 mediating centrosome biogenesis to anchor RGCs during DNA replication. Finally, behavior analysis indicated that fast fork speed led to an anxiety-like behavior in mice. Altogether, our results illuminate an unrecognized role about DNA fork speed in corticogenesis.

Key words: DNA fork speed, MCMBP, Neurogenesis, p53, Radial glial cell

INTRODUCTION

The neocortex is a mammalian evolutionary advance that controls sensation, emotion, sleep, learning and memory et al activities (Kaas, 2019; Lui et al., 2011; Sousa et al., 2017). This complex structure is generated through a series of neurogenic events, during which DNA integrity maintenance is essential. Consequently, the regulation of DNA replication fork speed is central to neurogenesis (Kalogeropoulou et al., 2019; McKinnon, 2013). However, the potential role of DNA fork speed during cortical development remained largely unknown.

Cortial development begins with neural epithelial stem cells, which self-amplify actively to increase the population of neural progenitor cells at early stages, then transit into the primary type of NPCs named apical radial glial cells (RGCs) (Fernández et al., 2016; Kwan et al., 2012). Located in the ventricular zone (VZ), apical RGCs are highly polarized with a short apical process attached to the ventricular surface and a long basal process extending to the cortical surface (Kwan et al., 2012). Before neurogenesis or at the onset of neurogenesis, RGCs predominantly undergo symmetry divisions, producing two RGCs (Fernández et al., 2016; Keil et al., 2020; Kwan et al., 2012). Along with the neurogenesis, RGCs will gradually switch into asymmetry division to generate neurons directly, or vi intermediate progenitor cells (IPCs) of sub-ventricular zone (SVZ) to generate neurons indirectly (Fernández et al., 2016; Keil et al., 2020; Kwan et al., 2012).

DNA replication is a highly regulated process, involving the assembly of a pre-replicative complex at the origins of replication (Fragkos et al., 2015). The mini-chromosome maintenance proteins (MCMs) form a DNA replication complex (RC) that is evolutionarily conserved from yeast to human. It consists of MCM2-7 arranged in a hexmeric ring as a CDC45–MCM–GINS (CMG) helicase, which binds to the origins of replication (Forsburg, 2004; Kuipers et al., 2011). The MCM binding protein (MCMBP) is essential for MCM function as a chaperon, assisting in the assembling and unloading of MCM3-7 subcomplex, and subsequent nuclear import (Forsburg, 2004; Nishiyama et al., 2011). MCMBP can also stabilize MCM2-7 to maintain the

speed of RC movement and reduce errors generated during DNA replication (Saito et al., 2022; Sedlackova et al., 2020; Yadav and Polasek-Sedlackova, 2024).

Moreover, MCM2 can enter the nucleus and interact with MCM3-7 to form a potentially functional MCM complex (Ghosh et al., 2011; Yan et al., 1993). Without MCMBP, MCM3-7 subunits undergo degradation in the cytoplasm, leading to inefficient nuclear import (Saito et al., 2022; Sedlackova et al., 2020). Importantly, in proliferating cells, MCMs are maintained at high expression levels to ensure robust and faithfully replication of DNA by restraining the speed of the DNA replication fork (Yadav and Polasek-Sedlackova, 2024).

To understand the functional role of DNA fork speed in cortical development, we performed DNA fiber assay on RGCs and observed that fork speed was gradually increased over the course of neurogenesis, which was consistent with a reduction of *Mcmbp* expression levels over the same period. Then, we manipulated fork speed by conditional *Mcmbp* deletion from mouse embryonic brain, and thoroughly studied the *in vivo* consequences. We found that following *Mcmbp* deletion, DNA fork speed was accelerated in RGCs, leading to massive cell apoptosis, DNA damages, and p53 robustly activation at later neurogenesis stages. Unexpectedly, at early stages, deletion of *Mcmbp* did not induce cell apoptosis. Further, without *Trp53* and *Mcmbp*, DNA fork speed in RGCs was significantly faster than *Mcmbp* deletion alone, and drove many RGCs to gradually lose attachments to the surface of VZ, thus acquired outer-RGCs like features especially highly proliferative abilities. Finally, we investigated whether fork speed increasing in embryonic brain development would affect adult mice behavior. All together our results reveal a previously unknown role of DNA fork speed in cortical development and its subsequent impact on adult mice behavior.

RESULTS

Mcmbp expression decreases and DNA fork speed increases over the course of neurogenesis

During cortical development, the RGCs undergo a transition from early symmetric to later asymmetric division (Gotz and Huttner, 2005). To characterize DNA replication fork speed during this transition, we performed DNA fiber assay to quantify DNA replication fork dynamics in RGCs isolated from cortices at two key stages-E12.5 mainly for symmetric division generating two RGCs, and E16.5 mainly for asymmetric division generating one RGC and one neuron (**Figure 1A**). To label actively progressing replication forks *in vivo*, two different halogenated nucleotides IdU (5-Iodo-2′-deoxyuridine) and CldU (5-Chloro-2′-deoxyuridine) were sequential delivered in utero by IP injections. These nucleotides are incorporated into the nascent DNA strands, thus providing information about replication (**Figure 1A**). Comparative analysis indicated that the fork speed was significantly increased by approximately 1.18 folds from E12.5 to E16.5 (**Figure 1B**).

MCMBP can assemble MCM2-7 to form a stable protein complex as a DNA helicase to separate duplex DNA strands and to maintain DNA fork speed during the DNA replication process (Sedlackova et al., 2020). (**Figure 1C**, left panel), indicating that MCMBP may play a role in maintaining DNA fork speed under physiological conditions. Therefore, to examine the expression pattern of *Mcmbp* gene, we utilized spatial and temporal transcriptome data generated during mouse neurogenesis (Telley et al., 2019), and found that the expression of *Mcmbp* was highest at E12, and then gradually decreased along 48 hours cortical development to E15 (**Figure 1C**, right panel). To corroborate this result, we performed western blot (WB) on the cortices from 4 embryonic stages (E10.5, E12.5, E15.5 and E17.5) and 3 postnatal time points (Postnatal day 0, day 10 and 20) (**Figure 1D**). Consistent with RNA expression results (**Figure 1C**), at protein level, the expression of MCMBP was also gradually decreased (**Figure 1D**), underlying an inverse relationship with DNA fork speed accompany corticogenesis. Moreover, MCMBP expression was much higher at symmetric division

stages (E10.5-E12.5) compared with asymmetric division stages (E15.5-E17.5) (**Figure 1D**) in line with identified fork speed changing results (**Figure 1B**). Further, we re-analyzed publicly available single-cell RNA expression data from E14.5 embryonic mouse cortex (Loo et al., 2019), and identified that *Mcmbp* expression was significantly enriched at neural progenitor cells, but not in post-mitotic neurons (**Figure S1A**, Cluster 11, *p-adj* = 3.21E-23).

Taken together, these results suggest that the *Mcmbp* expression is enriched in progenitor cells and exhibits a negative relationship with fork speed changing during corticogenesis, and thus might be important for regulating DNA fork speed in RGCs.

Mcmbp is essential for cortical development and fork speed maintenance

To understand MCMBP function *in vivo*, we generated *Mcmbp* conditional knock-out (KO) mice using *Emx1-Cre* (Gorski et al., 2002), a transgenic line that mediates Cre recombination in cortical RGCs starting at E10.5 (**Figures S1B and C**). Interestingly, *Mcmbp*$^{fl/fl}$*; Emx1-Cre* (cKO) mice were viable at birth and on postnatal day 3 (P3), cKO mice exhibited under development characterized by red skin and smaller body size (**Figure 1E**). Western blotting results confirmed that compared with controls, cKO mice showed significantly reduced expression of MCMBP in the cortices at E15.5 by ~43.98%, E16.5 by~55.29%, and P4 by ~53.34% respectively (**Figure 1F**). Further, at both P4 and P8, two different postnatal brain maturation stages, cKO mice showed 26.09% and 32.56% decrease in cortical area (**Figures 1G and S1D**), 15.71% and 21.90% decrease in cortical plate thickness (**Figures 1H and S1E**) to the controls.

To investigate whether neuronal subtypes were affected after *Mcmbp* deletion, we analyzed cortical layer markers at P4 and P8. The results showed that deeper layer neurons markers TBR1(Hevner et al., 2001) and TLE4(Shen et al., 2006) expressed in layer (L) 6 were not significantly changed in terms of number or laminar location (**Figures 1I and S1F-G**). However, upper layer (L2-4) neuron markers BRN2 (McEvilly et al., 2002) and LHX2 (Bulchand et al., 2001; Monuki et al., 2001) expressed were reduced significantly by 41.99% for BRN2, 41.11% for LHX2 at P4

(**Figure 1I**), and 55.26% and 63.10% for BRN2 and LHX2 at P8 respectively (**Figure S1G**). Together, although cortical layer organization was not affected following *Mcmbp* deletion, the number of upper layer neurons were significantly reduced.

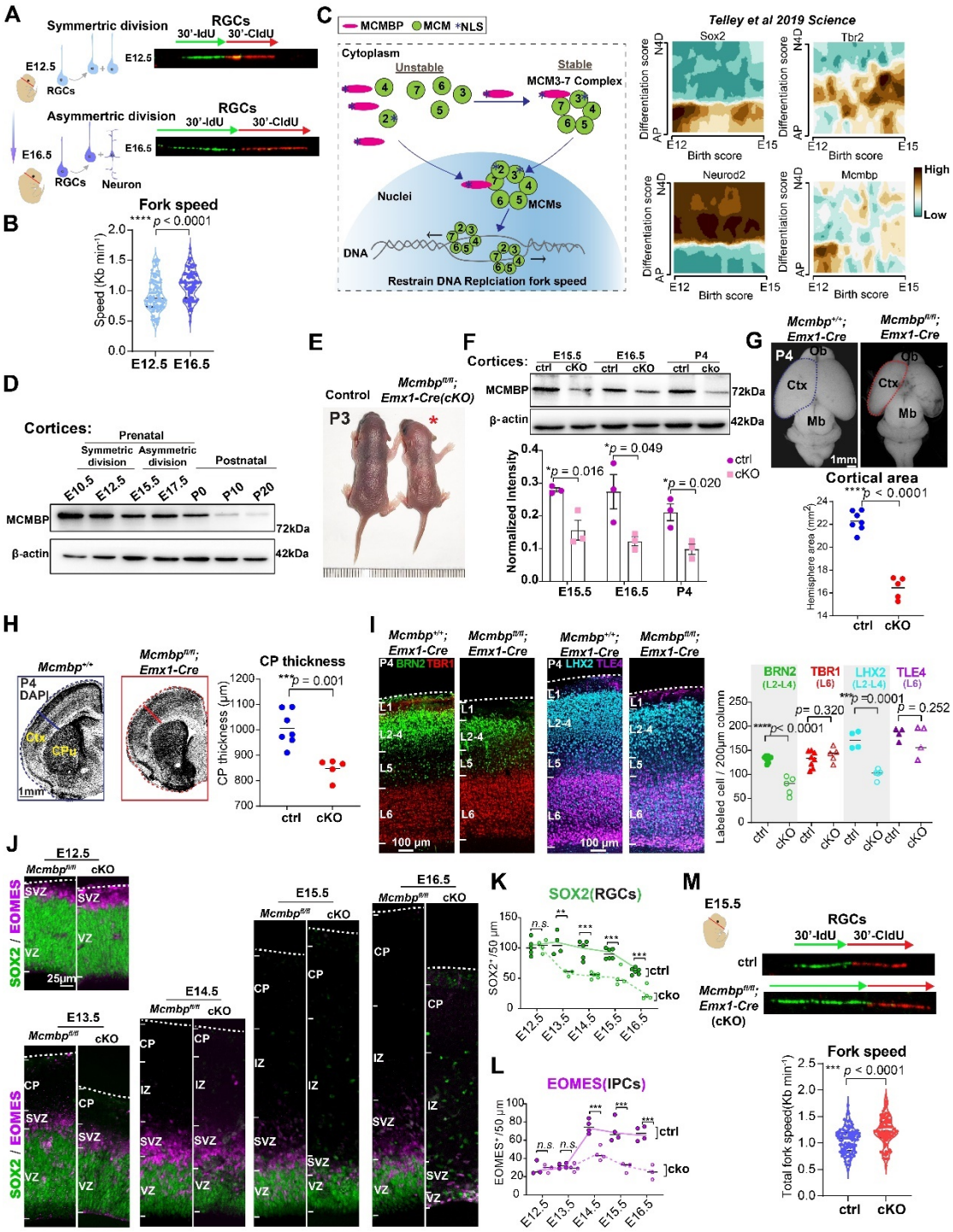

Figure 1. *Mcmbp* deletion in neural progenitors leads to DNA fork speed increase and microcephaly.

(A) (Left panel) Schematic map showing symmetric division and asymmetric division mode. (Right panel) Representative images of DNA fork fibers on isolated neural progenitors from

E12.5, and E16.5 cortices respectively.
(B)DNA fork speed and symmetry comparison analysis at early-E12.5 and later stages-E16.5 respectively.
(C) (Left panel) Schematic map showing MCMBP assembly, stabilize, and export MCM3-7 into cell nuclei to forming MCMs with MCM2, then restrain DNA replication fork speed. NLS means nuclei localization signal (Right panel) Spatial temporal expression of *Mcmbp* from apical to basal position, and from E12.5 to E15.5.
(D) Western blot analysis showing *Mcmcbp* expression pattern at prenatal and postnatal stages during cortex development.
(E) Representative images of cKO mouse and littermate control at P3. The red star indicates cKO mouse.
(F) Western blot analysis showing downregulation of *Mcmcbp* expression in the E15.5, E1.6.5 and P4 cortex.
(G) (Top) Dorsal view of $Mcmbp^{+/+}$; *Emx1-Cre* and $Mcmbp^{fl/fl}$; *Emx1-Cre* (cKO) P4 brain. (Bottom) The cortical area was significantly reduced in cKO compared to littermate control (ctrl).
(H) (Top panel) DAPI staining coronal sections of $Mcmbp^{+/+}$ and cKO P4 brain. (Bottom panel) Cortical plate thickness was significantly reduced in cKO compared to littermate controls.
(I) (Left panel) Immunostaining of layer markers BRN2, TBR1, LHX2 and TLE4 in in P4 brain of $Mcmbp^{+/+}$; *Emx1-Cre* and cKO. (Right panel) Upper layer neurons were significantly reduced in cKO compared to the littermate controls.
(J) Immunostaining of apical progenitor marker SOX2 and intermediate progenitor marker EOMES in $Mcmbp^{+/+}$; *Emx1-Cre* and cKO from E12.5 to E16.5.
(K) SOX2+ cell number analysis indicated that there was no difference between ctrl and cKO at E12.5. However, since E13.5, SOX2 cells were significantly reduced and continued until E16.5.
(L) EOMES+ cell number analysis indicated that there was no difference between ctrl and cKO at E12.5 and E13.5. However, EOMES+ cells were significanly reduced from E14.5 to E16.5.
(M) DNA fiber analysis between control and cKO at E15.5, indicated that DNA fork speed was significantly increased in cKO.

RGCs give rise to deeper layer neurons first and then upper layer neurons, which is considered as a process of sequential neurogenesis (Kwan et al., 2012). Therefore, we quantified the number of RGCs from E12.5 to E16.5 (**Figure 1J**). SOX2-expressing aRGCs of cKO started to show a significant reduction in number at E13.5 (**Figure 1K**). The number of EOMES-expressing intermediate progenitor cells (IPCs) first showed significant reduction at E14.5 of cKO (**Figure 1L**). Both apical RGCs and IPCs were mostly exhausted at E16.5, a stage for generating upper layer neurons (**Figures 1J-L**). Thus, deletion of *Mcmbp* leads to loss of NPCs, following a progressive manner. Noticeably, at both E15.5 and E16.5, some SOX2+ cells in cKO were detected outside

of VZ and SVZ, suggesting delamination of some RGCs after *Mcmbp* deletion (**Figures 1J**).

Finally, we performed fiber assay to assess DNA replication fork speed in cKO at embryonic E15.5, the results indicated that DNA fork speed was significantly increased following *Mcmbp* deletion (**Figure 1M**, ctrl mean=1.048 kb/min vs cKO mean= 1.217 kb/min).

Mcmbp deletion led to rapid apoptosis in RGCs during later asymmetric division stage

To examine whether apoptosis contributed to NPCs loss, we analyzed the level of activated caspase-3 in the cortices. We observed robust cleaved caspase 3 (CC3)-labeling at VZ, SVZ and intermediate zone (IZ) of E15.5 cKO cortex; however, only rare instances were found in the cortical plate (**Figure 2A**). To assess the timing of apoptosis, we used a dual pulse of thymidine analogs 5-ethynyl-2′-deoxyuridine (EdU) and 5-bromo-2′-deoxyuridine (BrdU), which are incorporated into DNA in S phase, to track NPCs fate. To label NPCs that had recently entered S phase, BrdU was given 4 hours before analysis at E15.5. BrdU-labeled NPCs entered S-phase in VZ and SVZ, similar between cKO and littermate controls (**Figure S2A**). However, compared to controls, fewer BrdU-labeled NPCs entered the S-phase of SVZ (**Figure S2A**). Furthermore, in cKO, BrdU+ cells were significantly colocalized with CC3 in both VZ and SVZ (**Figure S2B**), indicating NPCs underwent apoptosis rapidly following *Mcmbp* deletion. We then performed long-term tracking of S-phase cells, and EdU was given 24 hours before analysis at E15.5. In contrast to BrdU (**Figure S2B**, 6.67%), a majority of EdU+ NPCs had become apoptotic within 24 hours of S phase in cKO (**Figures S2C and S2D**, ~71.33%). Surprisingly, in cortical plate of cKO, we identified apoptotic signal in post-mitotic neurons (**Figure S2C**, white arrow), implying that *Mcmbp* deletion potentially led to accelerated NPCs differentiation.

By analyzing the progression of apoptosis, we found surprisingly that apoptosis was rarely detected in cortical zone at E12.5, a stage mainly for symmetric division,

within two days of *Emx1-cre* onset (**Figure 2B**). However, during the asymmetric division stages, apoptosis started to appear at E13.5 and showed a gradual increase pattern until E15.5, which is known to be a peak stage of neurogenesis. At E15.5, apoptotic cells were abundantly presented in the germinal zone, but absent from the subplate (SP) and CP. Surprisingly, at E16.5, only one day later, CC3 level was substantially reduced (**Figure 2B**). DNA DAPI-staining revealed a considerable amount of pyknotic nuclei, a result of chromatin condensation and a hallmark of apoptosis rarely found in controls (**Figure 2C**). In addition, we observed that pyknotic nuclei formed a clustering pattern (**Figure 2C**, red square), which is similar to the previous reports (Shi et al., 2019). Quantification of pyknotic nuclei revealed that the number of pyknosis was low at E12.5, but gradually increased from E13.5 to E15.5 within asymmetric stages, and then reduced dramatically at E16.5 (**Figure 2D**). These results implied that disruption of DNA replication fork speed during asymmetric but not symmetric division stages, leads to apoptosis.

Further, to investigate cell cycle progression, we used phospho-histone H3 (pHH3) staining to label M-phase cells and found that compared with controls, there were fewer RGCs at M-phase in both luminal-VZ and outside-VZ in cKO (**Figure S2E**). We further used Ki67 staining to label the cells throughout the cell cycle and 4 hours pulse of BrdU to label cells in the S-phase. Therefore, BrdU+Ki67- cells stand for those exiting from cell cycle and the analyzed results showed that 15.33% RGCs in cKO have been exited from cell cycle (**Figure S2F**). Additionally, after 24 h pulsed with EdU, a higher percentage of RGCs ~54.01% had been exited from cell cycle (**Figure S2G**) and failed to become post-mitotic neurons. These results indicated that RGCs in cKO were unable to progress through S-phase and exited from cell cycle process. Consistent with incompletion of S phase in cKO, fewer generated neurons were in the intermediate zone (IZ) (**Figure S2G**), where migrating neurons are mainly located.

Together, these data suggested that because of accelerated DNA fork speed, RGCs in cKO largely failed to complete cell cycle to become neurons at later neurogenesis stage, and underwent rapid apoptosis within 24 hours.

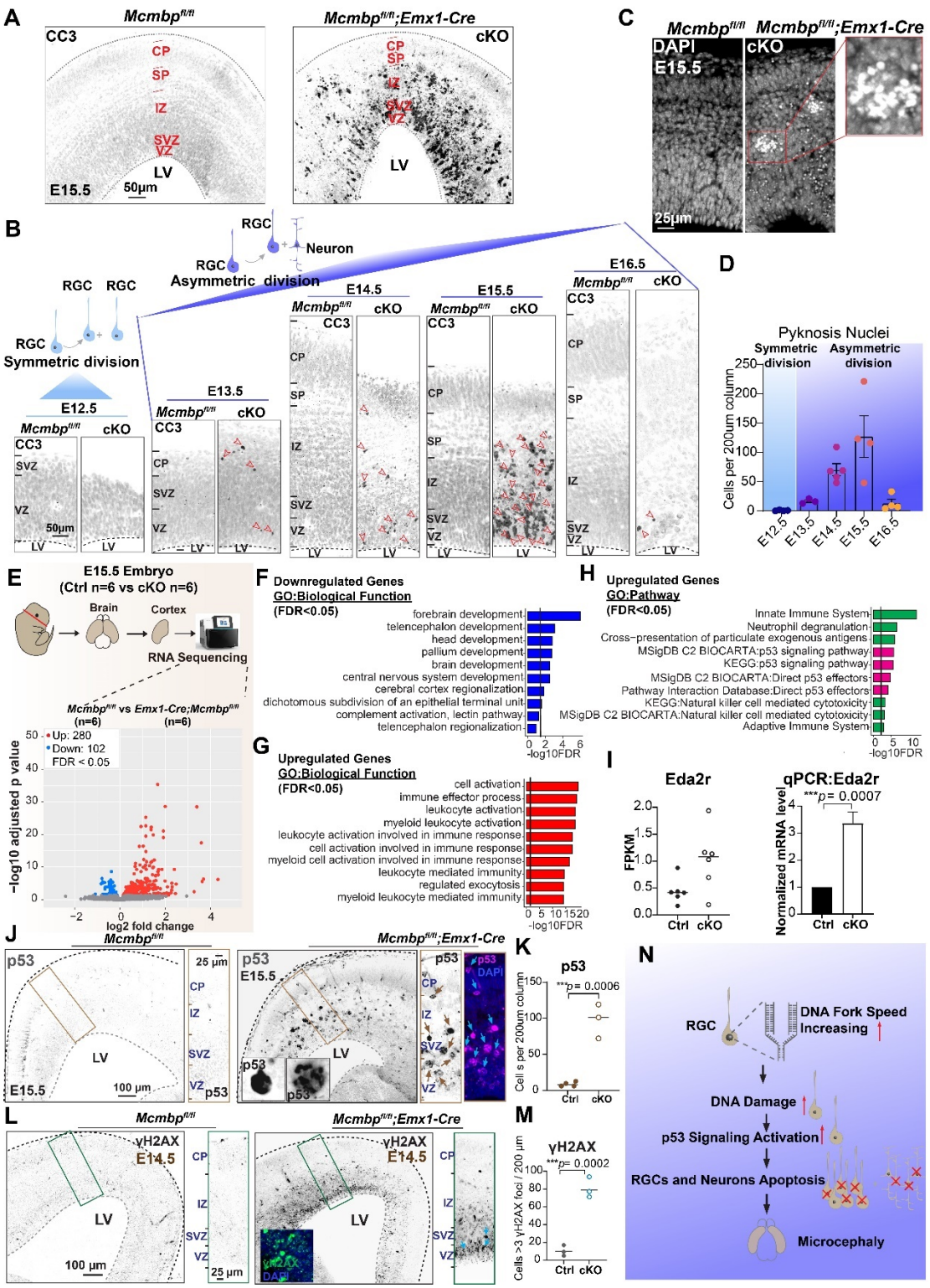

Figure 2. *Mcmbp* deletion in neural progenitors leads to rapid apoptosis, DNA damage and p53 upregulation within asymmetric division stages.

(A) CC3 immunostaining revealed extensive apoptosis in cKO at E15.5.

(B) CC3 immunostaining from E12.5 to E16.5 indicated that cell apoptosis was appeared from asymmetric division stage-E13.5 but not symmetric division stage-E12.5, and reached the peak at E15.5, which also coincdes with the peak for neurogenesis. Red arrow indicated apoptotic cell.

(C) (Top) DAPI staining revealed pyknotic nuclei in cKO cortical plate, cluster pyknotic nuclei were marked with red box.
(D) Quantification results indicated that the number of pyknotic nuclei was appeared from E13.5, and reached the peak at E15.5.
(E) Schematic map of RNA-seq process at E15.5 and volcano plot of differential expressed genes (DEGs) between cKO and control.
(F-G) GO biological function analysis of downregulated genes and upregulated genes in cKO respectively.
(H) GO pathway analysis of upregulated genes in cKO.
(I) Q-PCR results validated Eda2r high expression pattern in cKO.
(J-K) Immunostaining and quantification of p53 at E15.5, revealed p53+ cells were significantly increased in cKO.
(L-M) Immunostaining and quantification of γH2AX+ at E14.5, revealed γH2AX+ cells were significantly increased in cKO.
(N) Schematic model of deletion of *Mcmbp* induced acceleration of DNA replication fork speed on DNA damage, p53 signaling and cell apoptosis.

Mcmbp **deletion led to DNA damage and p53 activation**

To explore the genetic mechanisms underlying apoptosis induced by rapid DNA fork speed, we performed transcriptome analysis on dissected cortices (ctrl n=6 vs cKO n=6) at E15.5 (**Figure 2E**). Analysis of differentially expressed genes (DEGs) identified 279 up-regulated and 102 down-regulated genes in cKO (**Figure 2E**, Table S1). Further, Gene ontology (GO) analysis showed that the downregulated genes were significantly enriched in terms related to the forebrain development, while the upregulated genes were enriched in immune response related terms (**Figures 2F and G**, Table S2). Further, pathway analysis suggested that p53 mediated signal pathways are overrepresented (**Figure 2H**, 4/10) which indicated that upregulation of p53 has triggered cells undergoing apoptosis process. The expression of *Eda2r* has been found to be activated in p53 dependent cell death (Brosh et al., 2010). Among the top regulated genes, *Eda2r* was upregulated in cKO (**Figure 2I**), an increase that was verified by real-time PCR experiment (**Figure 2I**). Finally, we immunostained for stabilized p53 and found that the number of p53+ cells was much increased in E15.5 cKO and preferentially located in VZ and SVZ (**Figures 2J and K**, pink arrow).

Increased vulnerability to DNA damage may accompany the high speed of fork progression, which could induce the NPCs to undergo apoptosis following *Mcmbp*

deletion. To assess DNA damage during neurogenesis, we immuno-stained and quantified for DNA damage marker γH2AX at E14.5, E15.5 and E16.5 respectively. The results showed that number of γH2AX+ cells (>3 foci) in cKO was significantly increased compared to controls and such γH2AX signal was mainly enriched at VZ/SVZ where the NPCs mainly resided (**Figures 2L-M and S2H-I**). In particular, at E14.5, one day before the peak of apoptosis in cKO, DNA damage was highest with an average of 80 cells/200um with >3 γH2AX foci (**Figures 2L-M**) compared with E15.5 (40 cells/200um >3 foci) and E16.5 (40 cells/200um > 3foci) respectively (**Figures S2 H-I**).

All together, these results suggest that DNA damage was induced by rapid fork speed, which triggered p53-dependent apoptosis in RGCs following *Mcmbp* deletion (**Figure 2N**).

***Trp53/Mcmbp* co-deletion largely rescued microcephaly phenotype**

To further understand the role of p53 in mediating apoptotic response and the consequences of rapid fork speed in neurogenesis, we generated *Mcmbp/Trp53* conditional double mutants (*Mcmbp*$^{fl/fl}$; *Trp53*$^{fl/fl}$; *Emx1-Cre*, dKO). Surprisingly, analysis of dKO phenotypes at P3 showed that the body size and skin color were rescued to control (**Figure 3A**). At P8, brain size and cortical thickness were largely ameliorated (**Figures 3B and C**). Cortical layer analysis indicated that upper layer neurons (L2-4) were largely restored after removing p53 in cKO, while deep layer neurons (L5-L6) were comparable among controls, cKO and dKO (**Figures 3D-G**). Moreover, we observed LHX2+ cells that were dispersed in the cortical plate, and some of them were even in the deep layers of dKO (**Figure 3F**, white star), indicating potential defects in cortical neuron migration in dKO.

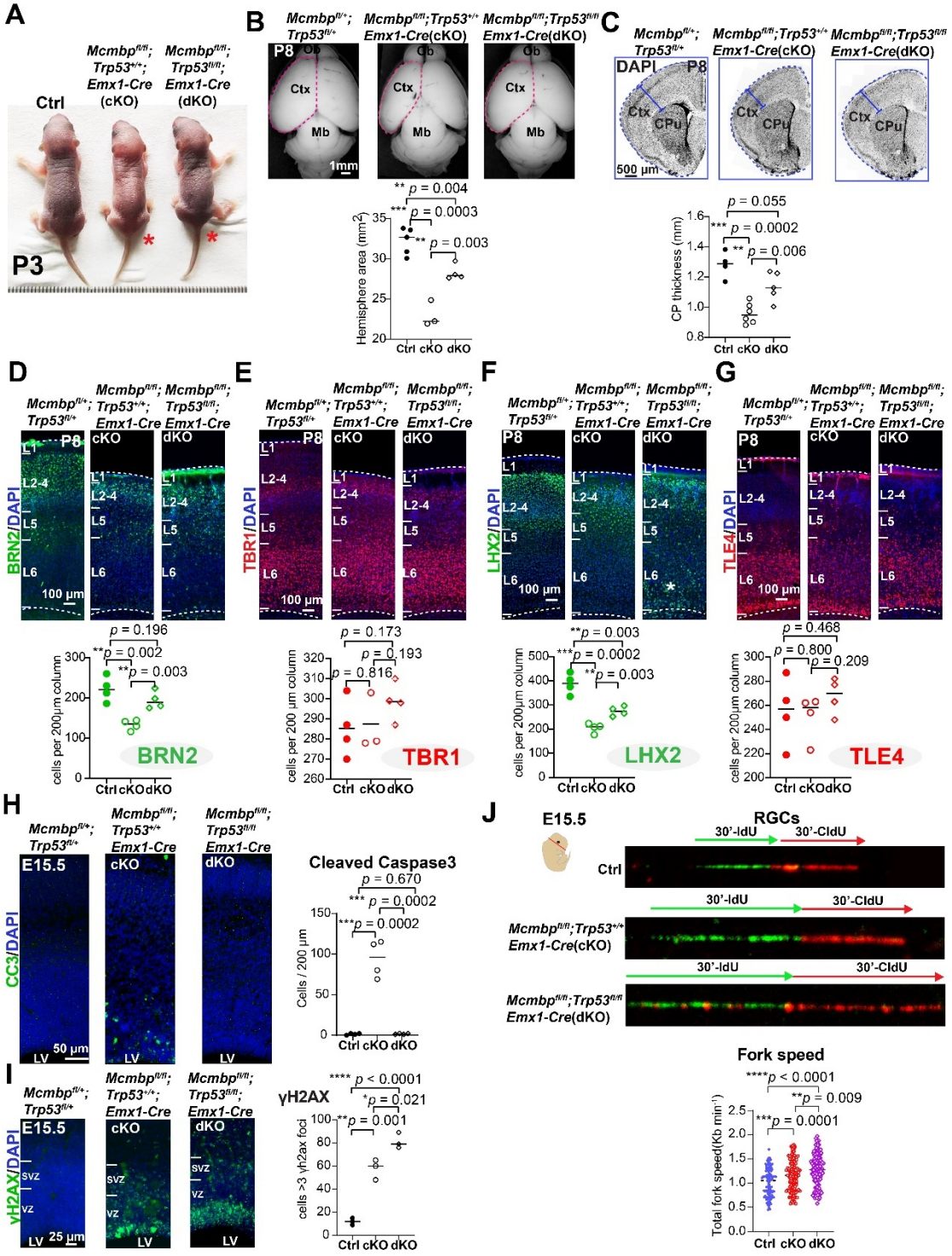

Figure 3. *Trp53/Mcmbp* co-deletion partially rescued microcephaly.

(A) Representative images of *Mcmbp*$^{fl/fl}$; *Emx1*(cKO), *Mcmbp*$^{fl/fl}$; *Trp53*$^{fl/fl}$; *Emx1*(dKO) mice, and littermate controls at P3. Red star indicates *Mcmbp* cKO and dKO.

(B) (Top) Dorsal view of control, cKO, and dKO brain at P4. (Bottom) Cortical area was partially rescued in dKO compared to littermate control (ctrl) and cKO.

(C) (Top panel) DAPI staining coronal sections of *Mcmbp* $^{fl/+}$; *Trp53* $^{fl/+}$, cKO and dKO P4 brain. (Bottom panel) Cortical plate thickness was rescued in dKO compared to littermate controls and cKO.

(D-G) (Top) Immunostaining of layer markers BRN2(D), TBR1(E), LHX2(F), TLE4(G) in *Mcmbp* $^{fl/+}$; *Trp53* $^{fl/+}$, cKO, and dKO P8 brain. (Bottom) Upper layer neurons BRN2, but not LHX2, were rescued in dKO, deeper layer neurons showed no differences compared to the cKO and controls.
(H) Immunostaining and quantification results of $CC3^+$ indicated that apoptotic cells were eliminated completely in dKO.
(I) Immunostaining and quantification results of γH2AX+ indicated that DNA damaged cells were significantly increased in dKO compared to the cKO and controls.
(J) DNA fiber analysis among control, cKO, and dKO at E15.5, indicated that DNA fork speed was significantly increased in dKO compared to the cKO and controls.

To investigate whether the rescued phenotype is due to apoptosis being prevented by the absence of p53, we verified that the number of CC3-labeling cells in dKO exhibited no differences to the controls (**Figures 3H**), indicating that apoptosis induced by *Mmcbp* deletion is p53-dependent. Next, we examined whether the DNA damage was persistent in dKO. The immunostaining results showed that the number of γH2AX (>3 foci) in dKO was significantly higher than the cKO (**Figure 3I**, dKO 81.33%, cKO 57.67%, ctrl 12%), suggesting that DNA damage induced by DNA fork speed is tolerant to the p53 deletion. However, interestingly, the number of phospho-(p) KAP1 positive cells, an ATM substrate and marker of heterochromatic double-strand breaks (DSBs) (Goodarzi et al., 2008), is fully rescued in dKO (**Figure S3**), suggesting that in the absence of p53, high fork speed mainly triggers single strand DNA breaks. Next, we sought to understand fork speed in dKO by performing fiber assay experiments. The analysis results showed that RGCs fork speed in dKO is significantly higher than cKO (**Figure 3J**), emphasizing that the RGCs undergoing apoptosis in cKO were results from uncontrolled fork speed.

Rapid fork speed led to massive RGCs detachment from ventricular zone, presenting oRGC-like features

Next, we sought to ask whether the progenitors were rescued in the absence of p53. Although the total number of SOX2+ apical RGCs was increased in dKO (**Figure 4A**), a massive of ectopic SOX2+ cells were localized outside of the VZ, especially in the IZ (**Figure 4B**). Consistent with the results of apical RGCs, the number of EOMES+ IPs

in dKO was significantly higher than that in cKO (**Figure 4C**), but slightly less than the controls (**Figure 4C**). Most of the increased IPs in dKO were ectopically located in the IZ (**Figure 4D**), suggesting that these ectopic IPs might be differentiated from displaced SOX2+ cells.

Further, to examine whether ectopically localized RGCs were detached from the surface of VZ progressively, we analyzed RGCs at early and late developmental stages including E13.5, E14.5, E15.5 and E17.5. The results showed that both SOX2+ RGCs and EOMES+ IPs exhibit a progressive increase in detachment during corticogenesis (**Figure S4**). Especially, at E17.5, close to the end of neurogenesis, there were still many SOX2+ RGCs that remained displaced at IZ (**Figure S4**).

According to the residing place, radial glial cells (RGCs) can be categorized into apical and basal RGCs respectively. Notably, basal RGCs, also named outer radial glial cells (oRGCs), are predominantly located at SVZ and rarely found in mouse species (Fietz et al., 2010; Hansen et al., 2010). This prompted us to ask whether those displaced progenitors exhibited oRGC like features. To address this, we performed double staining with RGCs marker SOX2 and oRGC marker HOPX (Thomsen et al., 2016) at E17.5 and detected the detached progenitors carrying SOX2+HOPX+ signals at extra-VZ (**Figures 4E-F**).

In addition, blood vessels are crucial for RGCs proliferation, differentiation, and migration process et al by providing nutrients, energy et al (Di Marco et al., 2020; Morimoto et al., 2024). With the use of isolectin-IB4 as a marker for blood vessel (Walchli et al., 2015) at E17.5, we verified that blood vessels exhibited an overgrown phenotype in dKO (**Figure 4G**). Consistently, the results of double staining with IB4 and HOPX indicated that in dKO cortex, blood vessels were surrounded with HOPX+ progenitor cells outside of VZ, supporting the critical roles of blood vessel during neurogenesis (**Figure 4H**).

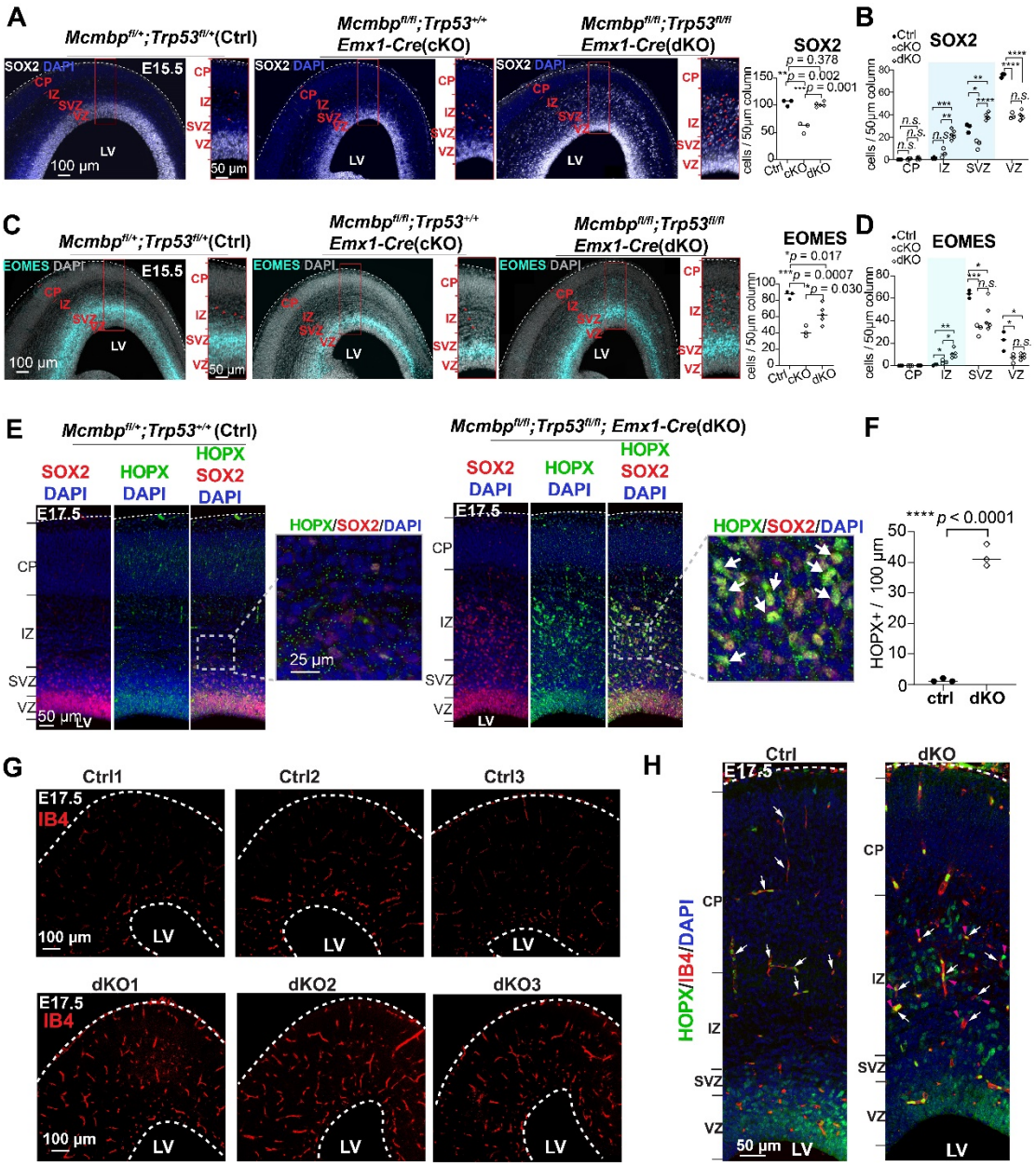

Figure 4. *Trp53/Mcmbp* co-deletion leads to delocalization of RGCs and IPCs.

(A) Immunostaining of E15.5 cortex revealed the number of SOX2+ (white color) cells in dKO were rescued to levels comparable to controls.

(B) Quantification of SOX2+ cells distributions revealed that SOX2+ cells were displaced in extra-VZ including SVZ and IZ in dKO.

(C) Immunostaining of E15.5 cortex revealed the number of EOMES+ (cyan color) cells in dKO were higher than cKO, but less than controls.

(D) Quantification of EOMES+ cells distributions revealed that EOMES+ cells were displaced in IZ in dKO.

(E) Immunostaining of SOX2 and HOPX in E17.5 dKO and their littermate controls.

(G) IB4 staining to show blood vessel of cortex in E17.5 dKO and their littermate controls.

(H) IB4 and HOPX double staining to show blood vessel snug with HOPX+ progenitors in E17.5 dKO and their littermate controls. White arrow indicated IB4+ cells and pink arrow indicated HOPX+ cells.

***Trp53/Mcmbp* co-deletion shortens cell cycle and S phase length**

To analyze gene expression changes after removal of both *Trp53* and *Mcmbp*, we performed RNA-seq of the *Mcmbp*/*Trp3* dKO cortex with controls at E15.5. Totally, we identified 230 up-regulated and 56 down-regulated genes (**Figure 5A**, Table S3). Further, by intersected with DEGs identified from cKO, we found that only 19 upregulated genes and 4 downregulated genes are shared by both cKO and dKO respectively (**Figure 5B**, Table S4), indicating that after deleting *Trp53*, dKO can restore most of p53-dependent genes expression. Consistently, *Trp53* was significantly reduced in dKO, while *Eda2r* expression showed no difference between dKO and control (**Figure 5C**). GO analysis indicated that up-regulated genes are enriched in terms related to cell cycle process, cell division and chromosome segregation related terms (**Figure 5D**, top panel, TableS5). Molecular function analysis showed that upregulated genes are primarily involved in DNA replication, DNA helicase activity et al (**Figure 5D**, bottom panel, TableS5). These results suggest that apoptotic cells in cKO primary arise from dysregulated DNA replication during the S-phase.

To quantify cell cycle status in dKO, we performed flow cytometry analysis (FACS) using propidium iodide (PI), a DNA-labelling dye, to quantify the cell cycle phase of NPCs at E14.5 (**Figure 5E**). The FACS results suggested that in dKO, the percentage of cells in S-phase was significantly reduced, while the percentage of cells in both G1 and G2/M phases were comparable with controls (**Figure 5E**). Taking fork speed into consideration, we hypothesized that accelerated DNA replication fork speed leads to shortening of S phase duration, which in turn, reduces the percentage of S phase cells. Therefore, we performed a short-term dual pulse of EdU (2 hours) and BrdU (30 min) at E14.5 to quantify the length of cell cycle and S phase respectively. We found that the length of S phase was reduced by 12.04% in dKO (**Figure 5F**), confirming that rapid fork speed shortens the length of S phase. Because of this, the total cell cycle duration was also reduced by 11.21% (**Figure 5F**), indirectly reflecting that dKO NPCs were

prone to be proliferating continuously.

Further, long-term single pulse of EdU (24 hours) was applied at E15.5 and analysis of Ki67+EdU+ proliferating cells revealed that percentage of Ki67+EdU+ is significantly higher than controls (**Figures 5G-H**), and majority of those proliferating cells were the SOX2+ RGCs (**Figure 5I**). More importantly, we observed that detached SOX2+ RGCs with both Ki67 and EdU signals, indicating their capability to proliferate (**Figure 5I**). Consistent with the results of Ki67+EdU+, there was a significant increase in PHH3+ cells in the extra-VZ in E15.5 dKO (**Figure 5J**). Moreover, an increase about PHH3+ cells was also observed in the luminal VZ of dKO compared to cKO (**Figure 5J**).

Taken together, in dKO, the rapid DNA fork speed shortens the duration of the S phase and potentially leads RGCs to detach from their resident place VZ to proliferate in IZ in a progressive manner during cortical development.

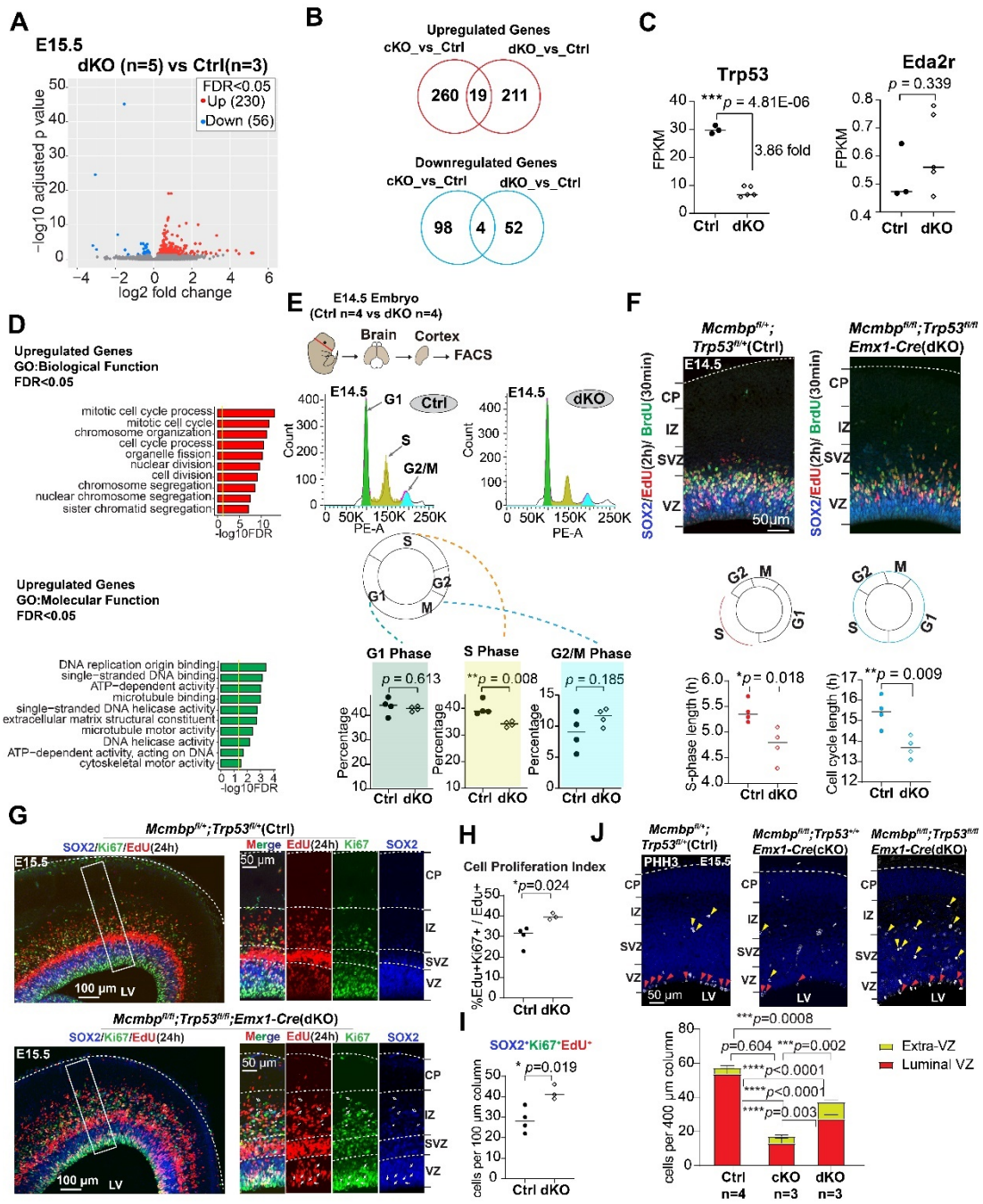

Figure 5. Single cell analysis in *Mcmbp/Trp53* dKO to identify expression profile of de-attached progenitors.

(A) Volcano plot showing differential expressed genes between controls and dKO.

(B) Venny plot showing little number of overlapped upregulated and downregulated genes between cKO and dKO.

(C) Gene expression plot with FPKM values showing that p53 expression was downregulated in dKO, while its target gene Eda2r expression was similar between dKO and controls.

(D) GO biological and molecular function analysis with upregulated genes.

(E) (Top) schematic map of the cell cycle analysis process at E14.5. (Middle) cell cycle distribution plots in control and dKO. (Bottom) Quantification of proportions of G1, S, and

G2/M phase in control and dKO indicating that S phase cells were significantly decreased in dKO.
(F) Analysis of E14.5 cortex following a 2-hour pulse of EdU (red) and a 0.5-hour pulse of BrdU (green), and quantitative results indicated that both S phase and whole cell cycle length were reduced in dKO.
(G) Analysis of E15.5 cortex following a 24-hour pulse of EdU (red), arrow indicated that SOX2+ NPCs at S phase was undergoing proliferating in dKO.
(H-I) Quantification of S phase cells (H) and related SOX2+ cells(I) between control and dKO.
(J) Quantification of M phase cells between control, cKO and dKO.

MCM3-p53-PCNT pathway regulates RGCs attachment to the surface of ventricular zone

To explore the molecular mechanism about RGCs detachment from VZ, we performed WB experiments on whole cell lysates with antibodies against MCM2-7 subunits (**Figures 6A**). Consistent with previous findings (Saito et al., 2022; Sedlackova et al., 2020), MCM2-7 subunits expression level exhibited a reduced pattern in cKO and dKO, but not in Emx1-*Trp53*cKO (**Figures 6A and B**). In fact, MCMBP sustained stabilization of MCM complex in the cytoplasm. In line with the results of whole cell lysates, in cKO and dKO, MCM2-7 subunits were downregulated in both the cytoplasm and nuclei, and MCM3 was again the only significantly reduced MCM subunit in dKO (**Figures S5A and B**).

MCM3 was specially downregulated in dKO not cKO (Figures 6A and S5A-B), implying that p53 might participate in regulation of MCM3 in RGCs. Co-immunoprecipitation (Co-IP) assays from embryonic cortex extracts verified that MCM3 interacts with p53 *in vivo* (**Figure 6C**). Previous studies have shown that MCM subunits participated in centriole duplication during cell cycle process by interacting with Plk1, a protein for centrosome maturation, at centrosome (Knockleby and Lee, 2010; Stuermer et al., 2007), however, the molecular mechanism by which MCM3 mediates centrosome biogenesis in RGCs is unknown. To identify whether MCM3 interacts with centrosome proteins, we performed Co-IP assays with the centrosome maker pericentrin (PCNT) and the results showed that MCM3 can interact with PCNT (**Figure 6D**). Further, we confirmed that PCNT can interact with p53 (**Figure 6E**).

Together, these results implied that MCM3-PCNT-P53 might form a functional complex to coordinate DNA replication and centriole function in neurogenesis. Normally, in WT, most of the mitotic cells at the VZ surface contained two PCNT foci (**Figure 6F**, two PCNT 95%, one PCNT 3.75%, none PCNT 1.25%), however, in the cKO, only 66.25% mitotic cells containing two PCNT foci and the percentages of one or none PCNT foci were significantly increased (**Figure 6F**, one PCNT 22.50%, none PCNT 11.25%). Importantly, in dKO, the percentage of two PCNT foci was significantly reduced to 23.75% more than cKO accompany by increased with no PCNT foci (**Figure 6F**, one PCNT 23.75%, none PCNT 30%), indicating that p53 deletion aggregated dysfunction of centriole duplication after deleting *Mcmbp*.

Centrosome is a major microtubule-organizing centers (MTOC) and indispensable for cell division, which consists of the cilium, distal appendages, subdistal appendages, centriole, and microtube (**Figure 6G**). Then, we performed WB to examine which component was affected by deletion of MCMBP and p53 (**Figure 6G**). The quantification results showed that CEP83 for distal appendage, PCNT for centriole, and ARL13B for cilium were all downregulated in both cKO and dKO, and subsequent p53 deletion further enhanced the repression effects (**Figure 6H**). In fact, ARL13B is a marker for primary cilia and essential for polarized radial glial scaffold formation (Higginbotham et al., 2013). In control, ARL13B labeled cells were uniformly distributed along the surface of VZ, whereas in cKO, they were brokenly distributed, and further dramatically reduced in dKO (**Figure 6I**). These results indicated that RGCs were detached from the VZ surface progressively due to selectively disruption of centrosome components following DNA fork speed acceleration. However, increased DNA fork speed did not affect subdistal appendage and microtubule markers' expression (**Figure 6H**).

Since VZ is a niche for radial glial cells (RGCs), which exhibits apical-basal polarity and are anchored to the apical surface of VZ, depending on the centrosome, primary cilia and N-cadherin proteins et al. N-cadherin (NCad) is a member of the calcium-dependent adhesion molecular family, mediating homotypic and heterotypic

cell-cell interaction (Miyamoto et al., 2015). At the surface of dKO-VZ, we observed a decrease in Ncad immunostaining (**Figure S5C**), indicating that loose interactions make RGCs were susceptible to be delocalized from the VZ.

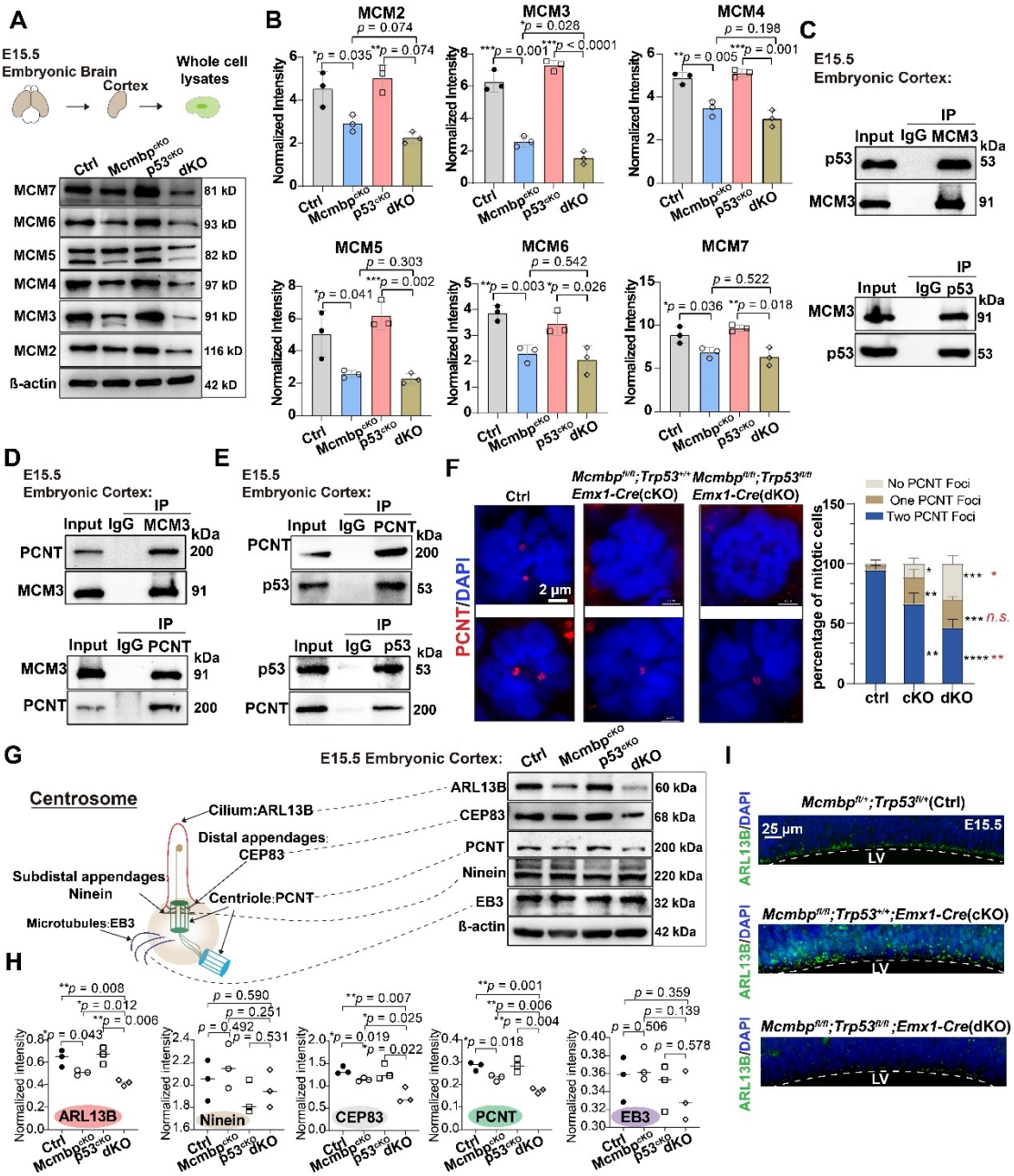

Figure 6. MCM3-p53-PCNT signaling coordinates DNA fork speed and centrosome biogenesis in progenitors.

(A) Western blotting on whole cell lysates and quantitative analysis identifying MCM3 as the only gene significantly repressed in dKO.

(B) Immunostaining of the MCM3 and quantitative analysis identifying nuclear MCM3 expression was downregulated in cKO.

(C) Co-immunoprecipitation between MCM3 and p53 in embryonic mouse cortex using MCM3 and p53 as bait, respectively.

(D) Co-immunoprecipitation between MCM3 and PCNT in embryonic mouse cortex using MCM3 and PCNT as bait, respectively.
(E) Co-immunoprecipitation between p53 and PCNT in embryonic mouse cortex using p53 and PCNT as bait, respectively.
(F) (Left) centrosome marker PCNT immunostaining in control, cKO and dKO. (Right) Quantitative analysis percentages of two PCNT foci, one PCNT foci, and none PCNT foci respectively.
(G) Schematic map of centrosome components and western blotting analysis on their representative markers.
(H) Quantitative analysis of western blotting results for centrosome components.
(I) Representative images of the cilium marker ARIL13B at luminal VZ in E15.5 control, cKO, and dKO.

Taken together, in wild type attached RGCs, during DNA replication, MCMBP-assisted export of MCM2-7 subunits into DNA nuclei initiates DNA replication and restrains DNA fork speed, meanwhile, the MCM subunit MCM3 interacts with p53 and centrosome protein PCNT to coordinate centrosome biogenesis with DNA synthesis process.

Rapid fork speed in neurogenesis results in anxiety-like behavior in adult mice

Finally, we were wondering whether the increase in DNA fork speed during cortical neurogenesis would exert effects on adult mouse behavior. Firstly, we examined brain size at postnatal 45 days (P45), adult dKO brain morphology was very similar to control, however brain size was still smaller than control, and both were bigger than cKO (**Figure 7A**). Then, we checked largest white matter fiber-corpus callosum (CC) integrity in the mouse brain, connecting left and right hemisphere as the major commissural pathway (Fitsiori et al., 2011). We found that consistent with the microcephaly phenotype in cKO, CC thickness was thinner and exhibited bifurcated phenotype (**Figure 7B**), while in dKO, CC phenotype was rescued and comparable with controls (**Figure 7B**).

Then we performed behavioral analysis on three-months-old mice using 3D Mouse behavior system (Huang et al., 2021). Principal component analysis (PCA) with kinematic features indicated that cKO group was clearly separated from the other two

groups (**Figure 7C**). Interestingly, dKO was clustered and slightly separated with control group indicating that rescued brain size can restore behavior to wild type in some degree (**Figure 7C**). Consistent with PCA results, open filed trajectory results showed that dKO trajectories were much like those of control compared with cKO (**Figure 7D**). However, both cKO and dKO exhibited a reduction in time spent in open field center compared with controls (**Figure 7E**), indicating that although brain size, white fiber like CC, and et al were recused, rapid fork speed during cortical development resulted in anxiety-like behavior in the long run (**Figure 7E**). Further, we took advantage of 3D Mouse analysis system to systematically dissect the detailed phenotypes. For body morphology, dKO showed much similarity to controls on body length and angle, both of which were higher than cKO (**Figure 7F**), and consistent with identified body phenotype at P3 (**Figure 3A)**. For natural behaviors, overall cKO showed much difference compared with control and dKO (**Figure 7G**). For example, cKO had a very high frequency in grooming, and a low frequency in sniffing, rising, and rearing (**Figure 7G**). In contrast, dKO showed no differences from controls on grooming and rising (**Figure 7G**), but presented a relatively low and high frequency on sniffing and rearing respectively (**Figure 7G**), indicating possibly abnormal brain function in dKO. Further, in terms of movement energy, and speed, most of the analyzed phenotypes showed much similar between dKO and controls including tail speed, and tail tip energy (**Figure 7H**).

Together, these data suggested that fork speed acceleration during cortical development may play an impact on brain maturation, and subsequent natural behavior at adult stage. However, future studies are necessary to understand how DNA fork speed impacts brain function during neuron maturation process, especially in cortical circuit development.

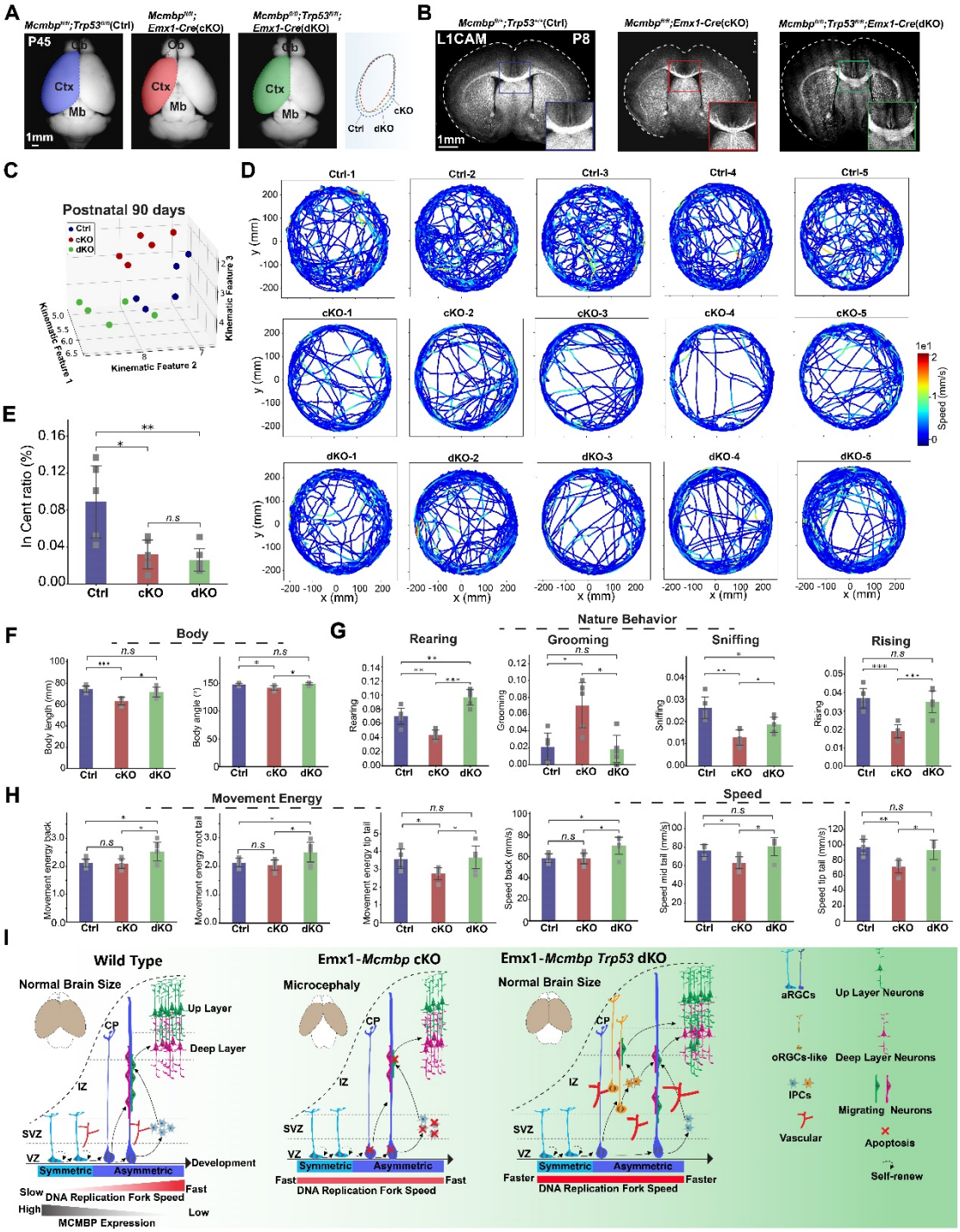

Figure 7. Fork speeding acceleration leads to an anxiety-like behavior in *Mcmbp* cKO and *Mcmbp/Trp53* dKO.

(A)Images of control, cKO, and dKO brains at P45.

(B)Immunostaining of L1cam to show corpus callosum in P8 control, cKO, and dKO.

(C) PCA analysis of kinematic features in controls, cKO, and dKO.

(D) Track records of open field assay from 5 controls, 5 cKO, and 5 dKO.

(E) Bar plots of in center ratio in controls, cKO, and dKO.

(F) Bar plots of body length and angel in controls, cKO, and dKO.

(G) Natural behavior analysis in controls, cKO, and dKO.

(H) Bar plots of movement energy, and speed in controls, cKO, and dKO.

(I)The proposed model for the DNA fork speed roles during neurogenesis. During cortical development, DNA fork speed has gradually increased (shown as a red gradient). This progression is initiated and restrained through the DNA replication complex-MCMs, which is assembled, stabilized and exported by MCMBP. In contrast to the fork speed progression, the expression of MCMBP is gradually decreased throughout the neurogenesis. Consequently, after deletion of *Mcmbp* in the early stages using Emx1-Cre, fork speed was increased (light red) in RGCs, which leading to massive cell apoptosis, and resulted in microcephaly phenotype. In the absence of *Mcmbp* and *Trp53*, although the brain size is largely rescued, DNA fork speed was unexpectedly increased (red color) and faster than deletion of *Mcmbp* alone, resulting in many RGCs detached from the VZ and became oRG-like cells (orange color) at the outside of VZ. As a result, the blood vessel was overgrown in dKO (*Mcmbp/Trp53* co-deletion), providing energy to the oRG-like cells potentially.

DISCUSSION

In cortical neurogenesis, maintaining genome stability and integrity is essential for generating a functional brain (McKinnon, 2017). Especially, DNA replication is the basis for duplicating a complete genome when neural stem cells undergo proliferation and differentiation into daughter cells. Therefore, interference with genes involved in DNA duplication process during neurogenesis could lead to neurodevelopmental disorders. For example, the *Topbp1* gene is required for DNA replication initiation, and its absence results in a striking defect in the development of mammalian cortex and cerebellar (Lee et al., 2012). DNA replication S phase length in RGCs has been shown a change from long to short during transition from RGCs symmetric to asymmetric division (McKinnon, 2013). However, none of the studies have tried to understand whether DNA replication fork speed would regulate RGCs fate in the neurogenesis.

In this study, we identified DNA fork speed as a key regulator of RGC fate in neurogenesis. MCMBP was highly expressed at early stages when RGCs were mainly undergoing symmetric division, and its expression then significantly declined during the later asymmetric division stages (**Figures 1C and D**). Consistently, we found that DNA fork speed was faster in RGCs with asymmetric division than those with symmetric division. To investigate DNA fork speed roles in neurogenesis, we generated *Mcmbp* cKO mice, and identified that DNA fork speed was increased in RGCs following *Mcmbp* deletion. This acceleration led to widespread DNA damage, p53

activation, and cell apoptosis in cKO mice at asymmetry division stages, resulting in a microcephaly phenotype. Further, in the absence of both *Mcmbp* and *Trp53*, although mouse brain size was largely rescued, DNA fork speed was faster than deletion of *Mcmbp* alone and stimulated RGCs detaching from VZ to the IZ acquiring oRGC like features. Thus, these results strongly supported the model that DNA fork speed acts as an engine and needs to be tightly regulated and restrained during cortical neurogenesis (**Figure 7I**). More interestingly, slowing DNA fork speed has also been shown to regulate cellular plasticity and improve reprogramming efficiency for pluripotent stem cells into totipotent like cells (Nakatani et al., 2022). It is also worthwhile to investigate the effects and related mechanisms of slowing fork speed in RGCs during cortical development.

Mechanistically, MCMBP is an important chaperon for the assembly, stabilization, and translocation of DNA replicative helicase- MCM complex, thus adjusting the pace of DNA fork speed to safeguard genome (Sedlackova et al., 2020). Without *Mcmbp* in RGCs, the expression of the MCM subunits was downregulated, resulting in dysregulation of DNA fork speed. Furthermore, without both *Mcmbp* and *Trp53*, RGCs fork speed was increased further and faster than cKO. This finding contrasts with the previous studies that have shown that removing p53 would reduce DNA fork progression (Klusmann et al., 2016; Lindström et al., 2022). Our co-IP experiments further demonstrated that p53 interacts with MCM3, implying that in the absence of MCMBP, p53 may protect MCM3 from degradation.

Centrosome duplication is necessary to synchronize with DNA replication to drive cell cycle progress (Bettencourt-Dias and Glover, 2007), however the underlying mechanism remains largely unknown. In fact, centrosome number and components were disrupted both in cKO and dKO, indicating that DNA fork speed regulation and centrosome biogenesis was required cooperation between MCM3 and p53 during cell cycle. Notably, both p53 and MCM3 can interact with the centrosome protein PCNT. Thus, after completing DNA replication at the S phase, the centrosome is duplicated and ready for chromosome segregation in the later phase of cell cycle. Besides that,

centrosome can regulate RGCs division mode through mitotic spindle direction (Gruber et al., 2011; Thornton and Woods, 2009). These results suggested that accelerated fork speed may change mitotic spindle orientation to favor asymmetric division by regulating centrosome behavior.

Surprisingly, RGCs with fast fork speed were retained in dKO, and were de-attached from VZ and dispersed into extra-VZ regions along with the brain development. Of note, the *Sas-4* gene, also known as *Cenpj* a key gene for centrosome biogenesis, knocking out *Sas-4* and *Trp53* simultaneously would also induce a similar phenotype-massive RGCs de-localizing at extra-VZ regions (Insolera et al., 2014). However, in contrast to the *Mcmbp*, *Sas-4* induced ectopic RGCs were the same with apical RGCs in terms of limited proliferative and differentiative abilities (Insolera et al., 2014). Because of the fast fork speed, displaced RGCs induced by *Mcmbp and p53* deletion were in a highly proliferative status, and strongly expressed oRG marker HOPX. To some extent, those characters had shown some similarities to those of human oRG cells especially highly proliferation abilities (Dehay et al., 2015), a key factor contributing to the expansion of human brain size since divergence from chimpanzee evolutionarily (Mora-Bermudez et al., 2022).

Blood vessel overgrowth in dKO suggests that running a proliferative RGCs required energy input continuously. Paradoxically, angiogenesis is an independently process, and only at later stages, angiogenesis will be affected by factors such as VEGF signaling produced by RGCs (Karakatsani et al., 2019). Vascular structures have preferentially contacted proliferative cells to modulate cell cycle process (Di Marco et al., 2020). Therefore, how displaced RGCs with accelerated fork speed are contacted by vascular filopodia is worth to investigate in future.

In summary, our study reveals a novel mechanism by which DNA fork speed not only regulates RGCs fate but also mediates RGCs attachment through the cooperation between DNA replication and centrosome biogenesis via MCM3-p53-PCNT pathway to significantly advance our understanding of the roles of genome stability and integrity in cellular plasticity regulation.

STAR★Methods

Key Resources Table

REAGENT or RESOURCE	**SOURCE**	**IDENTIFIER**
Antibodies		
Rabbit monoclonal anti-Ki67	Cell Signaling Technology	Cat# 9129S RRID:AB_2687446
Phospho-Histone H3 (Ser10)	Cell Signaling Technology	Cat#9701S RRID: AB_331535
Rat Monoclonal anti-SOX2	Invitrogen	Cat# 53-9811-82 RRID:AB_2574479
Rabbit Polyclonal anti-TBR1	Affinity	Cat# DF2396 RRID:AB_2839603
Mouse Monoclonal anti-BRN2/POU3F2	Santa Cruz Biotechnology	Cat# sc-393324 RRID:AB_2737347
Rabbit Polyclonal anti_LHX2	Millipore	Cat# ABE1402 RRID:AB_2722523
Mouse Monoclonal anti-TLE4	Santa Cruz Biotechnology	Cat# sc-365406 AB_10841582
Rabbit Monoclonal anti-P53(7F5)	Cell Signaling Technology	Cat# 2524S RRID:AB_331743
Rabbit Monoclonal anti-Phospho-Histone H2A.X (Ser139)	Cell Signaling Technology	Cat# 9718S RRID:AB_2118009
Rabbit Polyclonal anti-Cleaved	Cell Signaling Technology	Cat# 9661S RRID:AB_2341188

Caspase-3 (Asp175)		
Rabbit Polyclonal anti- phospho-KAP-1 (Ser824)	Bethyl	Cat# A300-767A RRID:AB_669740
Rabbit anti-IBA1/AIF1	Wako	Cat# 019-19741 RRID:AB_839504
Rat Polyclonal anti-ADGRE1/F4/80	Abcam	Cat# ab6640 RRID:AB_1140040
Mouse Monoclonal anti-N-cadherin	BD	Cat# 610920 RRID:AB_398236
Mouse Monoclonal anti-BrdU	BD	Cat# 347580 RRID:AB_400326
Rat Monoclonal anti-BrdU	Abcam	Cat# ab6326 RRID:AB_305426
Mouse Monoclonal anti-BrdU	Invitrogen	Cat# B35128 RRID:AB_2536432
Mouse Monoclonal anti-Beta Actin	Proteintech	Cat# 66009-1-Ig RRID:AB_2687938
Rabbit Polyclonal anti-MCM2	Proteintech	Cat# 10513-1-AP RRID:AB_2142131
Rabbit Polyclonal anti-MCM4	Proteintech	Cat# 13043-1-AP RRID:AB_2142293
Rabbit Polyclonal anti-MCM5	Proteintech	Cat# 11703-1-AP RRID:AB_2235162
Rabbit Polyclonal anti-MCM7	Proteintech	Cat# 11225-1-AP RRID:AB_22997584

Mouse Monoclonal anti-MCM3	Santa Cruz Biotechnology	Cat# SC-390480 N/A
Mouse Monoclonal anti-MCM6	Santa Cruz Biotechnology	Cat# SC-393618 AB_2885187
Rabbit Polyclonal anti-MCMBP	Invitrogen	Cat# PA5-58410 RRID:AB_2643815
CEP83	Proteintech	Cat# 26013-1-AP RRID:AB_2880334
NINEIN	Santa Cruz Biotechnology	Cat# SC-376420 RRID:AB_11151570
EB3	Proteintech	Cat# 23974-1-AP RRID:AB_2879385
Mouse Monoclonal anti-p-vimentin	Enzo	Cat# ADI-KAM-CC249-E RRID:AB_2039681
Rabbit Polyclonal anti-ARL13B	Proteintech	Cat# 66009-1-Ig RRID:AB_2060867
Rabbit Polyclonal anti -Pericentrin	Abcam	Cat# ab4448 RRID:AB_2060867
Rabbit Monoclonal anti - Pericentrin	Abcam	Cat# ab220784 N/A
Rat Monoclonal anti- Neural Cell Adhesion Molecule L1(L1CAM)	Millipore	Cat# MAB5272 RRID:AB_2060867
Mouse Monoclonal anti-PCNA	Proteintech	Cat# 60097-1-Ig RRID:AB_2236728
Alexa Fluor 594 AffiniPure Donkey Anti-Rabbit	Jackson	Cat# 711-585-152 RRID:AB_2340621

Alexa Fluor 594 AffiniPure Donkey Anti-Rat	Jackson	Cat# 712-585-153 RRID:AB_2340689
Alexa Fluor 488 AffiniPure Donkey Anti-Mouse	Jackson	Cat# 715-545-150 RRID:AB_2340846
Alexa Fluor 594 AffiniPure Donkey Anti-Mouse	Jackson	Cat# 715-585-150 RRID:AB_2340854
Alexa Fluor 488 AffiniPure Donkey Anti-Rabbit	Jackson	Cat# 711-545-152 RRID:AB_2313584
Alexa Fluor 488 AffiniPure Donkey Anti-Rat	Jackson	Cat# 712-545-150 RRID:AB_2340683
Alexa Fluor 647 AffiniPure Donkey Anti-Rat	Jackson	Cat# 712-605-153 RRID:AB_2340694
Anti-rabbit IgG, HRP-linked Antibody	Cell Signaling Technology	Cat# 7074 RRID:AB_2099233
Anti-mouse IgG, HRP-linked Antibody	Cell Signaling Technology	Cat# 7076 RRID:AB_11179080
Chemicals, Peptides, and Recombinant Proteins		
DMEM/F12	Gibco	Cat# C11995500BT
Penicillin-Streptomycin	Gibco	Cat# 15140122
B27 supplement	Gibco	Cat# 12587010
N2 supplement	Gibco	Cat# 17502048
EGF	Stemcell	Cat# 78006

bFGF	Stemcell	Cat# 78003
Heparin	Stemcell	Cat# 07980
Papain	Stemcell	Cat# 07465
Laminin	Siama-Aldrich	Cat# 114956-81-9
Poly-d-lysin	Siama-Aldrich	Cat# P3655
Adhesive Slides	Servicebio	Cat# G6012-1
DEPC-treated water	Biosharp	Cat# BL510A
DAPI	Invitrogen	Cat# 62248
antifade mounting medium	Vector Labs	Cat# H-1000
Citrate	Servicebio	Cat# G1202
normal donkey serum	Jackson	Cat# 017-000-121
bovine serum albumin	Sigma	Cat# SRE0096
protease inhibitor mixture	Roche	Cat# 4693116001
RIPA buffer	Beyotime	Cat# P0013B
Protein A/G magnetic Beads	MedChemExpress	Cat# HY-K0202
DPBS	Gibco	Cat# C14190500CP
EdU	Sigma	Cat# 61135339
BrdU	Sigma	Cat# 59143
IdU	Sigma	Cat# 54422
CIdU	Sigma	Cat# 50908
Protease K	Sigma	Cat# V900887
AF488 azide	Lumiprobe	Cat# 11830
Sulfo-Cyanine3 azide	Lumiprobe	Cat# A1330
Non-Fat powdered milk	BBI	Cat# A600669-0250
Immobilon transfer membrane	Millipore	Cat# IPVH00010

AMPure XP Beads	Beckmen	Cat# A63880
Critical commercial assays		
RNAsimple Total RNA Extraction Kit	TIANGEN	Cat# DP419
AceQ Universal SYBR qPCR Master Mix	Vazyme	Cat# Q511-03
RNase-Free DNase Set	QIAGEN	Cat# 79254
BCA Protein assay Kit	BIOMIKY	Cat# MK043A
Novex™ ECL chemiluminescence substrate Kit	Invitrogen	Cat# WP20005
HiScript III All-in-one RT SuperMix Kit	Vazyme	Cat# R333-01
AceQ Universal SYBR qPCR Master Mix Kit	Vazyme	Cat# Q511-02
GLOBINclear ™ Mouse/Rat Kit	Invitrogen	Cat# AM1981
VAHTS mRNA-seq v3 Library Prep Kit	Vazyme	Cat# NR611
SeekOne® DD S3 Microarray Kit	SEEKGENE	Cat# K00202-0201
SeekOne® DD Single-Cell Purification Kit	SEEKGENE	Cat# K00202-0205

Experimental Models: Organisms/Strains		
Mouse: *Mcmbp*$^{fl/fl}$	Gempharmatech Co.,Ltd	N/A
Mouse: *Trp53*$^{fl/fl}$	Jackson Laboratory	Cat#JAX:008462 RRID:IMSR_JAX:008462
Mouse: C57BL/6J	Kunming Institute o Zoology	N/A
Mouse:*Emx1*-cre	Jackson Laboratory	Cat#JAX:005628 RRID:IMSR_JAX:005628
Experimental Models: Cell Lines		
Neural progenitor cells	This paper	N/A
Software and Algorithms		
Trim Galore	Felix Krueger	https://github.com/FelixKrueger/TrimGalore
HISAT2 (v2.1.0)	Pertea et al., 2016	https://daehwankimlab.github.io/hisat2/
HTSeq-count	Anders et al., 2015	https://htseq.readthedocs.io/en/latest/
DESeq2 R package	Anders and Huber, 2010	https://bioconductor.org/packages/release/bioc/html/DESeq2.html
Cufflinks (v2.2.1)	Trapnell et al., 2013	https://cole-trapnell-lab.github.io/cufflinks/
imageJ	National Institutes of Health	https://imagej.nih.gov/ij/
GraphPad Prism 9	GraphPad	https://www.graphpad.com/
Other		
Vibratome-VT1000S	Leica	VT1000S
confocal microscope	Leica	TCS SP8

Super resolution microscopy	Abberior	STEDYCON
ABI7500 real-time PCR system	Applied Biosystems	ABI7500
FluorChem E	Proteinsimple	N/A

RESOURCE AVAILABILITY

Lead contact

Further information and requests for reagents may be directed to and will be fulfilled by Lead Contact Lei Shi (shilei@mail.kiz.ac.cn).

Materials availability

This study did not generate any unique reagents.

Data and code availability

All sequencing data were deposited at the NCBI Gene Expression Omnibus (GEO) under accession number GSE279962

Experimental Model and Subject Details

Ethics Statement

Animal research using mice was conducted according to the guidelines approved by the Animal Care and Use Committee of the Kunming Institute of Zoology, Chinese Academy of Sciences. The animals involved in this study were all from standard feeding environments and did not carry potential pathogens or parasites that would cause great interference to the results of the scientific experiments. *Mcmbp*$^{fl/fl}$ mice were generated by Jiangsu Gempharmatech Co., Ltd. C57BL/6J mice and Emx1-Cre (Gorski et al., 2002) were from Jackson Laboratory (Bar Harbor, ME, USA). C57BL/6J wild type mice were purchased from the Animal Center of Kunming Institute of Zoology, Chinese Academy of Sciences.

Cell lines

Neural progenitor cells were isolated from C57BL/6J, *Mcmbp* cKO, *Mcmbp/Trp53* dKO, and littermate control embryonic cortices including E12.5 and E15.5, and

cultured in Neurobasal Medium (GIBCO) supplemented with bFGF (STEMCELL), B27 (GIBCO), Glutamax (Invitrogen) and Penicilin/Streptomycin (Invitrogen) on glass coverslips were precoated with poly-L-ornithine and laminin.

Method Details

Generation of *Mcmbp* cKO mice

The *Mcmbp* gene has 5 transcripts. According to the structure of the *Mcmbp* gene, exon6-exon8 of the *Mcmbp*-201 (ENSMUST00000057557.13) transcript are targeted as the knockout region. This region contains 398bp coding sequence. Knocking out this region with CRISPR/Cas9 technology will result in disruption of protein function. The brief process is as show in Figure S1B: sgRNA was transcribed in vitro, the donor vector was constructed. Cas9, sgRNA, and donor constructs were microinjected into the fertilized eggs of C57BL/6J mice. Fertilized eggs were then transplanted into recipients to obtain positive F0 mice which were confirmed by PCR and sequencing. F1 generation mice was obtained by mating positive F0 generation mice with C57BL/6J mice. *Mcmbp* cKO mice were generated by crossing *Mcmbp*$^{fl/fl}$ mice with *Emx1*-Cre. *Mcmbp* cKO mice were identified through genotyping. The oligonucleotide primers used for genotyping are listed in Supplementary Table 6.

Isolation of mouse neural progenitor cells

We isolated single cell suspensions from mouse cerebral cortex and cultured them in proliferation medium consisting of DMEM/F12 (Gibco, C11330500BT), 2% B27 supplement (Gibco, 12587010), 1% N2 supplement (Gibco, 17502048), 20 ng/ml epidermal growth factor (EGF, STEMCELL, 78006), 10 ng/ml basic fibroblast growth factor (bFGF, STEMCELL, 78003), 1% penicillin/streptomycin (100 units/mL of penicillin and 100 μg/mL of streptomycin) (Gibco, 15140-122), 0.0002% heparin (STEMCELL, 07980). Cells were digested by papain (Worthington, Ls00319) at

passaging and seeded on 6-well culture plates pre-coated with 5μg/mL Laminin (Invitrogen,23017015) and 10 μg/mL poly-d-Lysine (Sigma, P3655).

Immunofluorescence staining and imaging

Brain tissues from mice at different developmental stages were collected and fixed in 4% paraformaldehyde (Acros Organics, AC416785000) for 24 h at room temperature. Subsequently embedded in 4% agarose and sectioned into 35-70 μm slices using a Vibratome (Leica, VT1000S). For immunostaining, antigen restoration was performed with citrate (Servicebio, G1202). Sections were washed three times with PBS and then incubated in PBS containing 0.5% Triton X- 100 (MACKLIN, TB24275) for 30 min. Following this, sections were blocked with PBS containing 5% normal donkey serum (Jackson, 017-000-121), 1% bovine serum albumin (Sigma, SRE0096), 0.1% glycine (BBI, A610235-0500), 0.1% lysine (MACKLIN, L812314) at room temperature for 1-2h. Sections were then incubated overnight at 4°C in primary antibodies diluted in blocking buffer. The next day, the sections were rinsed three times with PBS for 5 min each and then incubated with the corresponding fluorescent secondary antibodies for 2h at room temperature protected from light. Nuclei were labeled with DAPI (1:1000, Invitrogen, 62248). Stained sections were mounted with VECTASHILED Antifade Mountant (Vector Labs, H-1000). Finally, images were acquired using a confocal microscope (Leica, TCS SP8) and processed using ImageJ software (National Institutes of Health, NIH).

Primary antibodies: Mouse monoclonal anti-BRN2/POU3F2 (1:250, Santa Cruz Biotechnology, sc-393324); Rabbit polyclonal anti-TBR1 (1:250, Affinity, DF2396); Rabbit polyclonal anti-LHX2 (1:500, Millipore, ABE1402); Mouse monoclonal anti-TLE4 (1:100, Santa Cruz Biotechnology, sc-365406); Rabbit polyclonal anti-Pax6 (1:500, Invitrogen, 42-6600); Rat monoclonal anti-SOX2 (1:500, Invitrogen, 53-9811-82); Rabbit polyclonal anti-TBR2 / Eomes (1:500, Abcam, ab23345); Phospho-Histone H3 (Ser10) Antibody (1:500, Cell Signaling Technology, 9701S); Rabbit monoclonal anti-Ki67 (1:500, Cell Signaling Technology, 9129S); Rabbit monoclonal anti-P53(7F5) (1:500, Cell Signaling Technology, 25247S); Rabbit monoclonal anti- Phospho-

Histone H2A.X(Ser139) (1:500, Cell Signaling Technology, 9718S); Rabbit polyclonal anti-Cleaved Caspase-3 (Asp175) (1:500, Cell Signaling Technology, 9661S); Rabbit polyclonal anti-Phospho-KAP-1(Ser824) (1:500, Bethyl, A300-767A); Rabbit anti-IBA1/AIF1 (1:500, Wako, 019-19741); Rat polyclonal anti-ADGRE1/F4/80 (1:500, Abcam, ab6640); Mouse monoclonal anti-N-cadherin (1:250, BD, 610920); Mouse monoclonal anti-BrdU(1:250, Invitrogen, B35128); Rabbit polyclonal anti-MCM2(1:250, Proteintech, 10513-1-AP); Rabbit polyclonal anti-MCM4(1:250, Proteintech, 13043-1-AP); Rabbit polyclonal anti-MCM7(1:250, Proteintech, 11225-1-AP); Mouse monoclonal anti-p-vimentin(1:500, Enzo, ADI-KAM-CC249-E); Rabbit polyclonal anti-ARL13B (1:250, Proteintech, 66009-1-Ig); Rabbit Polyclonal anti-Pericentrin(1:250, Abcam, ab4448); Rat monoclonal anti-Neural Cell Adhesion Molecule L1(L1CAM) (1:500, Millipore, MAB5272); Secondary antibodies: Alexa Fluor 488 AffiniPure Donkey Anti-Rabbit (1:500, Jackson, 711-545-152); Alexa Fluor 488 AffiniPure Donkey Anti-Rat (1:500, Jackson, 712-545-150); Alexa Fluor 488 AffiniPure Donkey Anti-Mouse (1:500, Jackson, 715-545-150); Alexa Fluor 594 AffiniPure Donkey Anti-Rabbit (1:500, Jackson, 711-585-152); Alexa Fluor 594 AffiniPure Donkey Anti-Rat (1:500, Jackson, 712-585-153); Alexa Fluor 594 AffiniPure Donkey Anti-Mouse (1:500, Jackson, 715-585-150).

Protein extraction from cytoplasmic and cell nuclei

Nuclei and cytoplasmic proteins from mouse E15.5 embryonic cortex were extracted using the Beyotime kit (P0027). Fresh cortical tissue was obtained, and Cytoplasmic Protein Extraction Reagents A and B were mixed in a 20:1 ratio and added to the tissue. The mixture was incubated on ice for 15 minutes, then centrifuged at 15,000 x g for 5 minutes at 4°C to obtain the partial cytoplasmic protein fraction. The remaining pellet was resuspended in 200 μl of Cytoplasmic Protein Extraction Reagent A containing PMSF, mixed, and incubated on ice for 10-15 minutes. Subsequently, 10 μl of Cytoplasmic Protein Extraction Reagent B was added, mixed, and incubated on ice for 1 minute. The sample was then centrifuged at 15000 x g for 5 minutes at 4°C. The supernatants from both centrifugation steps were combined to yield the total

cytoplasmic protein fraction. For the pellet, completely remove any residual supernatant and add 50 μl of nuclei protein extraction reagent containing PMSF. Vortex at maximum speed for 15-30 seconds to ensure full dispersion of the pellet, then incubate on ice for 30 minutes, then vortex for 15-30 seconds every 3 minutes during incubation, subsequently, centrifuge at 15,000 x g for 10 minutes at 4°C. The resulting supernatant is the nuclei protein fraction.

Place the fresh cortical tissue in RIPA buffer (Beyotime, P0013B) supplemented with a protease inhibitor cocktail (Beyotime, P1005) and a phosphatase inhibitor (Beyotime, P1082). Homogenize the tissue using an ultrasonic homogenizer at 4°C for 5 cycles of 10 seconds each. Then, incubate the mixture on a shaker at 4°C for 10 minutes. Centrifuge at 15,000 x g for 10 minutes at 4°C, and collect the supernatant as the total protein solution.

Western Blotting Experiments

Protein samples were separated using 10% sodium dodecyl sulfate-polyacrylamide gel electrophoresis (SDS-PAGE) and transferred to PVDF membranes (Millipore, IPVH00010). The membranes were then blocked with 5% skimmed milk (BBI, A600669-0250) and incubated with the primary antibody at 4°C overnight. After TBST washing, the membranes were incubated for 1 h with horseradish peroxidase-labeled anti-mouse (1:1000, Proteintech, SA00001-1) and anti-rabbit (1:1000, Proteintech, SA00001-2) secondary antibodies. Chemiluminescence was detected using the SuperSignal West Pico PLUS kit (Thermo Fisher Scientific, 34579) according to the manufacturer's instructions.

The following primary antibodies were used for immunoblotting: Mcmbp (1:2000, Invitrogen, PA5-58410), MCM2 (1:1000, Proteintech, 66009-1-Ig), MCM3 (1:1000, Santa Cruz Biotechnology, SC-390480), MCM4 (1:1000, Proteintech, 13043-1-AP), MCM5 (1:1000, Proteintech, 11703-1-AP), MCM6 (1:1000, Santa Cruze Biotechnology, SC-393618), MCM7 (1:1000, Proteintech, 11225-1-AP), ARL13B(1:1000, Proteintech, 17711-1-AP), CEP83(1:1000, Proteintech, 26013-1-AP), PCNT(1:2000, Abcam, ab220784), NINEIN(1:1000, Santa Cruze Biotechnology,

SC376420), EB3(1:1000, Proteintech, 23974-1-AP), β-actin(1:2000, Proteintech, 66009-1-Ig), PCNA(1:1000, Servicebio, GB12010).

Co-immunoprecipitation assays

For co-immunoprecipitation (Co-IP), fresh cortical tissue was lysed in a buffer containing a proteinase inhibitor cocktail (Beyotime, P1005) and incubated on ice for 30 minutes. The lysate was centrifuged at 12,000 rpm for 10 minutes at 4°C, and the supernatant was carefully collected. Fifty microliters of Protein A/G magnetic beads (Medchemexpress, HY-K02002) were added for magnetic separation, and the supernatant was discarded. The beads were then resuspended in a solution containing primary antibodies against PCNT (Abcam, ab220784), MCM3 (Santa Cruz, SC-390480), and P53 (CST, 25247S) diluted to 20 μg/ml, and incubated with rotation overnight at 4°C. After magnetic separation and removal of the supernatant, the beads were resuspended in 50 μg of protein lysate and incubated with rotation overnight at 4°C. Following magnetic separation and supernatant removal, the beads were resuspended in SDS loading buffer, heated at 95°C for 7 minutes to denature the proteins, and then analyzed by 10% SDS-PAGE.

Real-time quantitative RT-PCR

Total RNA was extracted from mouse E15.5 embryonic cortex using total-RNA extraction kit (TIANGEN, DP429). cDNA was synthesized using the HiScript III All-in-one RT SuperMix Kit (Vazyme, R333-01). Quantitative real-time PCR (qPCR) was performed using the AceQ Universal SYBR qPCR Master Mix Kit (Vazyme, Q511-02) on an Applied Biosystems 7500 Real-Time PCR System (Waltham, MA, USA). The Ct values obtained for each gene were normalized by subtracting the Ct value of the reference gene 18sRNA. Normalized gene expression values are expressed as the relative quantity of Eda2r mRNA. The sequences of the oligonucleotide primers used for qRT-PCR amplification are detailed in Supplemental Table 7.

RNA Sequencing Library Construction and Illumina Sequencing

RNA purification, reverse transcription, library construction and sequencing were performed in Sequanta Technologies Co., Ltd at Shanghai according to the

manufacturer's instructions. The Globin mRNA was removed using GLOBINclear™ Mouse/Rat Kit (Invitrogen, AM1981). The non-Globin mRNA-focused sequencing libraries from 1μg total RNA were prepared using VAHTS mRNA-seq v3 Library Prep Kit (Vazyme, NR611). PolyA mRNA was purified from total RNA using oligo-dT-attached magnetic beads and then fragmented by fragmentation buffer. Taking these short fragments as templates, first strand cDNA was synthesized using reverse transcriptase and random primers, followed by second strand cDNA synthesis. Then the synthesized cDNA was subjected to end-repair, phosphorylation and 'A' base addition according to Illumina's library construction protocol. Then Illumina sequencing adapters were added to both size of the cDNA fragments. After PCR amplification for DNA enrichment, the AMPure XP Beads (Beckmen, A63880) were used to clean up the target fragments of 200-300 bp. After library construction, Qubit 3.0 fluorometer dsDNA HS Assay (Thermo Fisher Scientific) was used to quantify concentration of the resulting sequencing libraries, while the size distribution was analyzed using Agilent BioAnalyzer (Being, CHN). Sequencing was performed using an Illumina Novaseq 6000 following Illumina-provided protocols for 2x150 paired-end sequencing in Sequanta Technologies Co., Ltd.

Bulk RNAseq data analysis

Illumina reads were processed by FastQC quality control(https://www.bioinformatics.babraham.ac.uk/projects/fastqc/), trimming adapter sequences with Cutadapt tools(Martin, 2011) then remaining reads were mapped to the respective reference mouse genome(mm10) using HISAT2 2.1.0(Pertea et al., 2016). We quantified gene expression from the mapped reads using HTSeq-count (http://www-huber.embl.de/users/anders/HTSeq/doc/count.html) that obtained integer counts of mapped reads per gene. Cufflinks v2.2.1 was used to obtain FPKM expression values, using automatic estimation of the library size distributions and sequence composition bias correction (Trapnell et al., 2013). Differentially expressed genes were identified based on integer count data using R package DESeq2 version 1.36.0 (Anders and Huber, 2010), which determines DE by modeling count data using

a negative binomial distribution. Volcano plots are based on the DESeqAnalysis R package (Steinbaugh et al., 2018). For the list of differentially mRNA genes, we tested weather each had enriched GO terms in biological process and molecular functions using the ToppGene Suite (Chen et al., 2009). For ToppGene, only those functional annotation terms associated with the various sets of differentially expressed genes were clustered that were significantly enriched (Bonferroni correction, $p<0.05$) compared with the function annotation terms associated with the total population of genes.

Cell cycle analysis

Neural progenitor cells were isolated from E14.5 embryonic mouse cortex and fixed in precooled 70% ethanol and incubated at 4°C on a rocking platform for 48 hours. Following centrifugation at 1000 rpm to remove the 70% ethanol, the cells were washed twice with precooled PBS. Subsequently, the cells were incubated in the dark at 4°C for 30 minutes with 50 μg/mL propidium iodide (Sigma, P4170), 0.2% Triton X-100, and 100 μg/mL RNase A (Thermo Fisher Scientific, EN0531). The samples were analyzed on a Becton-Dickinson LSRFortessa flow cytometer (Franklin Lakes, NJ, USA), and data were processed using FlowJo software (FlowJo, LLC, Ashland, OR, USA).

Cell cycle kinetics calculation

Cell cycle kinetics were determined using the bi-thymidine labelling assay (Zhang et al., 2019). Pregnant mice with a designated time for E14.5, were injected with EdU (10 mg/ml, 100 μl / 100 g body weight) so that all S-phase cells were labelled at T=0 h. After T=1.5 h, the same pregnant mice were injected with BrdU (1 mg/ml, 100 μl / 100 g body weight), therefore, all cells in S phase were labelled. Animals were euthanized at T = 2 h and E14.5 embryos were collected immediately. Embryo sections were immune-stained using anti-BrdU antibody (Invitrogen, ab6326) and EdU staining solution consisting of 100 μL 1M tris, 100 μL 1M ascorbic acid, 794 μL PBS, 4 μL 1M $CuSO_4$ and 2 μL 4 mM Sulfo-Cyanine3 azide (Lumiprobe, A1330). Images were obtained on a Leica TCS SP8 inverted confocal microscope. The length of S-phase (Ts) and total length of cell cycle (Tc) were determined based on the relative number of cells that incorporated CldU and/or EdU. The equation used

was Ts = 1.5 h/(NCldU+EdU−/NCldU+EdU+) and Tc = Ts/(NCldU+EdU+/Ntotal)(Zhang et al., 2019).

DNA fiber assay

Neural progenitor cells were isolated from E12.5, E15.5 and E16.5 embryonic mouse cortex respectively, and cultured and labeled with 50 μM IdU and 50 μM CldU for 30 minutes each. Following centrifugation, the cells were resuspended in precooled PBS to a density of 1 × 10^5 cells/ml. Two microliters of the cell suspension were placed on one end of a microscope slide, and 10 μL of lysis buffer (0.5% SDS, 50 mM EDTA, 200 mM Tris-HCl, pH 7.4) was added. The slide was then tilted at 15°, allowing the drop to flow uniformly. The fibers were fixed with methanol-acetic acid (3:1) and denatured in 2.5 M HCl at 37°C for 20 minutes. After incubation with 1% BSA at room temperature for 1 hour, the slides were incubated overnight at 4°C with primary antibodies: Mouse monoclonal anti-BrdU (1:100, BD Biosciences, 347580) and Rat monoclonal anti-BrdU (1:100, Abcam, ab6326). Incubate Alexa Fluor 488 AffiniPure Donkey Anti-Mouse (1:500, Jackson, 715-545-150), Alexa Fluor 594 AffiniPure Donkey Anti-Rat (1:500, Jackson, 712-585-153) for 2 hours at room temperature. Finally, images were acquired using a confocal microscope and processed with ImageJ software, 1 μm of DNA fiber prepared by spreading corresponds to approximately 2.59 kb (Nieminuszczy et al., 2016). Statistical significance was determined by Student's t-test if comparing the two conditions, or by one-way ANOVA test for multiple comparisons.

Behavioural experiments

The Open Field Test was used to measure locomotor activity and anxiety-like behaviour in 3-month-old male mice (Kraeuter et al., 2019). We used the BAYONE BIOTECH BehaviorAtlas Analyzer-3D-Mouse Behavioural Device (Shenzhen Bayone BioTech), which allows for multi-viewpoint video acquisitionand was described in detail previously (Huang et al., 2021). The arena was used to monitor mouse behavior was a circular open field with a white plastic floor and transparent acrylic walls. The diameter of the base was 50 cm and the height of the walls was 30 cm. Mice were allowed to

explore the arena freely for 7 min and then 20 min of locomotor activity was recorded. The site was cleaned after each experiment. After all experiments were completed, the mice behavior could be observed by visualization software BehaviorAtlas Explorer. Subsequently, the data were analyzed by BehaviorAtlas Analyzer-Mouse analysis software.

Quantification and Statistical Analysis

The *Student's t-test* was used to determine the significant difference by comparing means between two groups of data. Paired data were from the same group but under different conditions was performed using an unpaired or paired two-tailed *Student's t-test*.

Code availability

We didn't generate specific codes for this study. All codes are based on customer software and available upon request.

ACKNOWLEDGMENTS

We thank the members of the Shi Laboratory for their discussions and comments on the manuscript. We would like to thank the Core Technology Facility of the Kunming Institute of Zoology, CAS for providing flow cytometry analysis and sorting. We also thank Shenzhen Bayone BioTech Co., Ltd for providing the BehaviorAtlas Analyzer-3D Mouse Behavioral Device and technical support. We are grateful to Guolan Ma and Shuangjuan Yang for providing technical support.

FUNDING

L.S. is supported by the Pioneer Hundred Talents Program of the Chinese Academy of Sciences and the Yunnan Revitalization Talent Support Program Young Talent Project. This study was supported by grants from the National Natural Science Foundation of China (32170630), Yunnan Applied Basic Research Projects (202201AS070043 and 202401AS070072), Science and Technology Major Project of Science and Technology of Department of Yunnan Province (202102AA100057), Spring City Project from Kunming Science and Technology Bureau (2022SCP007) to L.S. K.X. is supported by the joint special project for basic research between the Yunnan Provincial Science and Technology Department and Kunming Medical University (202101AY070001-269)

AUTHOR CONTRIBUTIONS

L.S. and J.C.I.B. conceived the study; L.S. designed the study; JH.W. performed mouse experiments, JH.W., YF. K., XZ. L., YL. T, and K.X. performed molecular biology experiments; L.S. performed bioinformatics analysis; L.S., and JH.W. prepared the figures; L.S., and JH.W. wrote the final manuscript.

DECLARATION OF INTEREST

The authors declare no competing interest.

Supplementary Figures

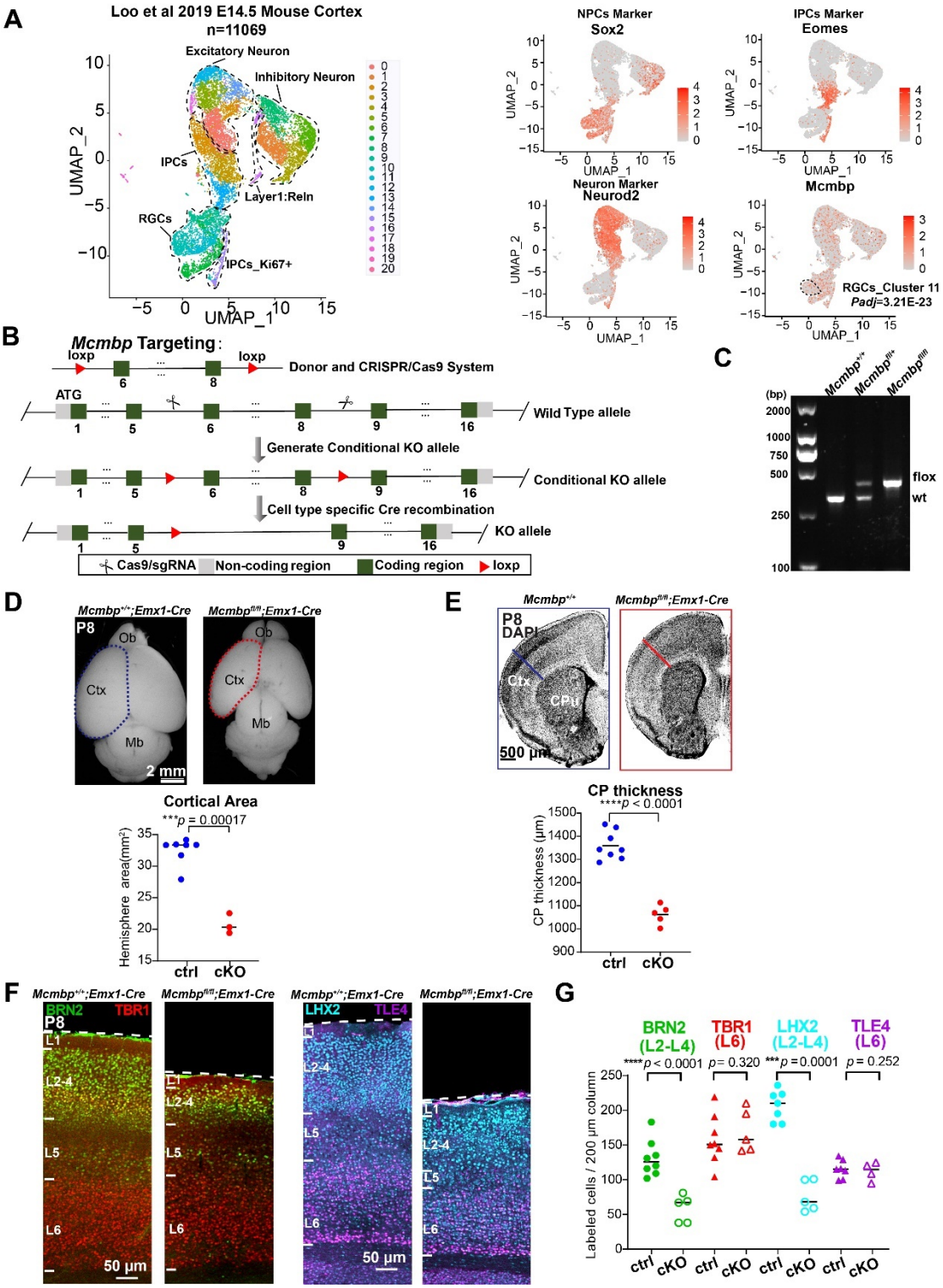

Figure S1. Generation of *Mcmbp* conditional knock-out mice. Related to Figure 1. (A) Uniform manifold approximation and projection (UMAP) plot showing cell types identified in the E14.5 mouse cortex. NPCs mark gene *Sox2*, IPCs mark gene *Eomes*, neuron marker gene *Neurod2*, and *Mcmbp* expression in the identified cell types.

(B) Schematic representation of the generation of Mcmbp conditional flox mice using CRISPR-Cas9 technology.

(C)PCR results of wild type, heterozygous and homozygous mice.

(D) (Left panel) Dorsal view of Mcmbp$^{+/+}$; Emx1-Cre and Mcmbpfl/fl; Emx1-Cre (cKO) P8 brain. (Right panel) Cortical area was significantly reduced in cKO compared to littermate controls (ctrl).

(E) (Left panel) DAPI staining coronal sections of Mcmbp$^{+/+}$ and cKO P8 brain. (Right panel) Cortical plate thickness was significantly reduced in cKO compared to littermate controls (ctrl).

(F) Immunostaining of layer markers BRN2, TBR1, LHX2 and TLE4 in Mcmbp$^{+/+}$; Emx1-Cre and cKO P8 brain.

(G) Upper layer neurons were significantly reduced in cKO compared to the controls (ctrl).

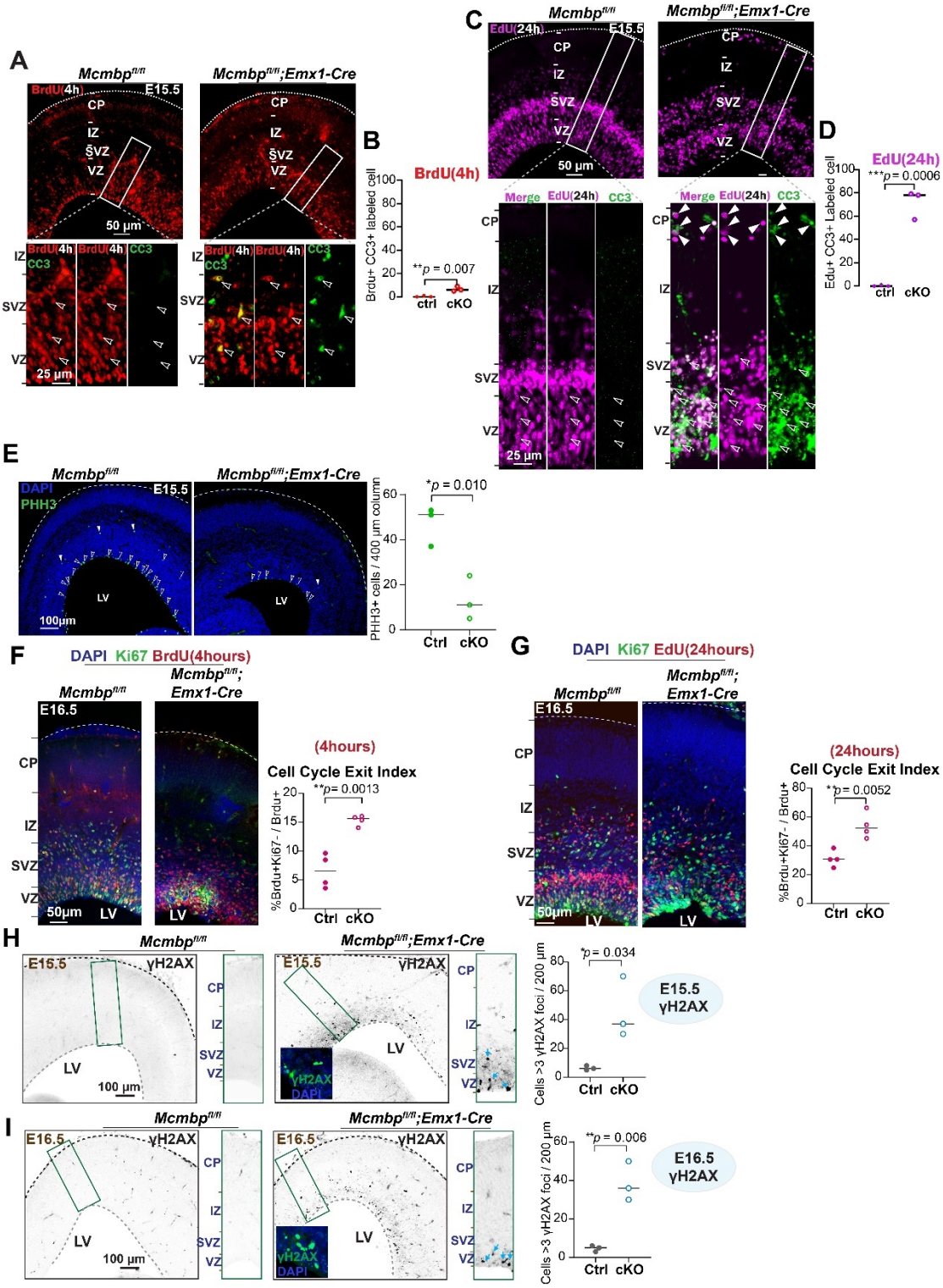

Figure S2. Robust apoptosis, pyknotic nuclei, cell cycle exiting, and DNA damage were present in neural progenitors following *Mcmbp* deletion. Related to Figure 2. (A) Analysis of E15.5 cortex following a 4-hour pulse of BrdU (red). CC3 staining (green) showed apoptosis in BrdU+ cells (open arrowheads) in Emx1-*Mcmbp*cKO, but not in control.

(B) Quantification results of BrdU+ and CC3+, indicated NPCs rapidly entered into the apoptosis process within 4 hours following *Mcmbp* deletion.

(C) Analysis of E15.5 cortex following a 24-hour pulse of EdU (magneta). CC3 staining (green) showed apoptosis in BrdU+ cells (open arrowheads) in Emx1-*Mcmbp*cKO, but rarely in control.

(D) Quantification results of EdU+ and CC3+, indicated a massive of NPCs entered into apoptosis process in cKO within 24 hours.

(E) Representative images and a quantification of M phase cells PHH3+ at E15.5.

(F) Representative images and a quantification of cell cycle exiting cells following BrdU pulse for 4 hours at E15.5.

(G) Representative images and a quantification of cell cycle exiting cells following EdU pulse for 24 hours at E15.5.

(H) Representative images and quantification of DNA damage cells γH2AX+ at E15.5.

(I) Representative images and quantification of DNA damage cells γH2AX+ at E16.5.

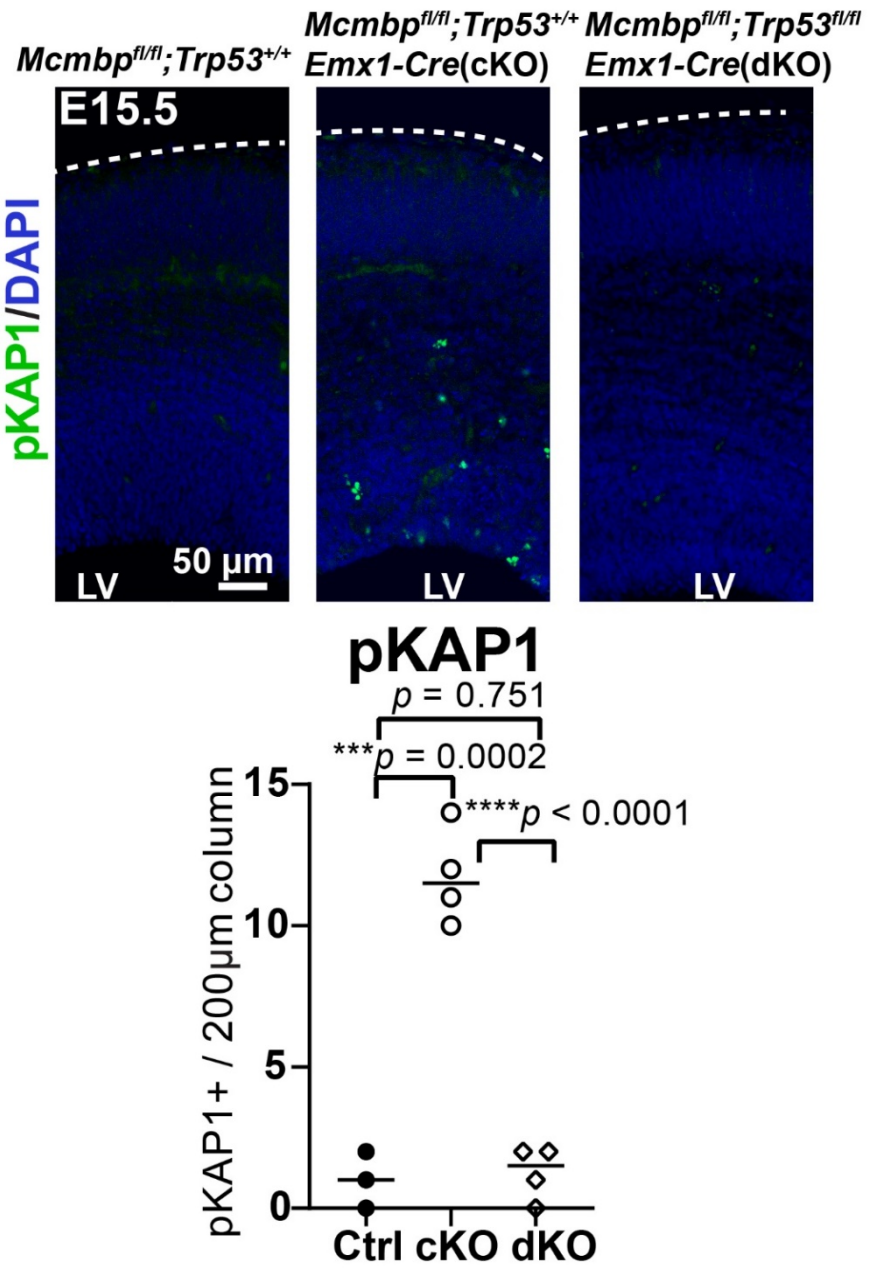

Figure S3. Representative images and quantification of DNA double strand break cells pKAP1+ at E15.5 *Mcmbp/Trp53* dKO cortex. Related to Figure 3.

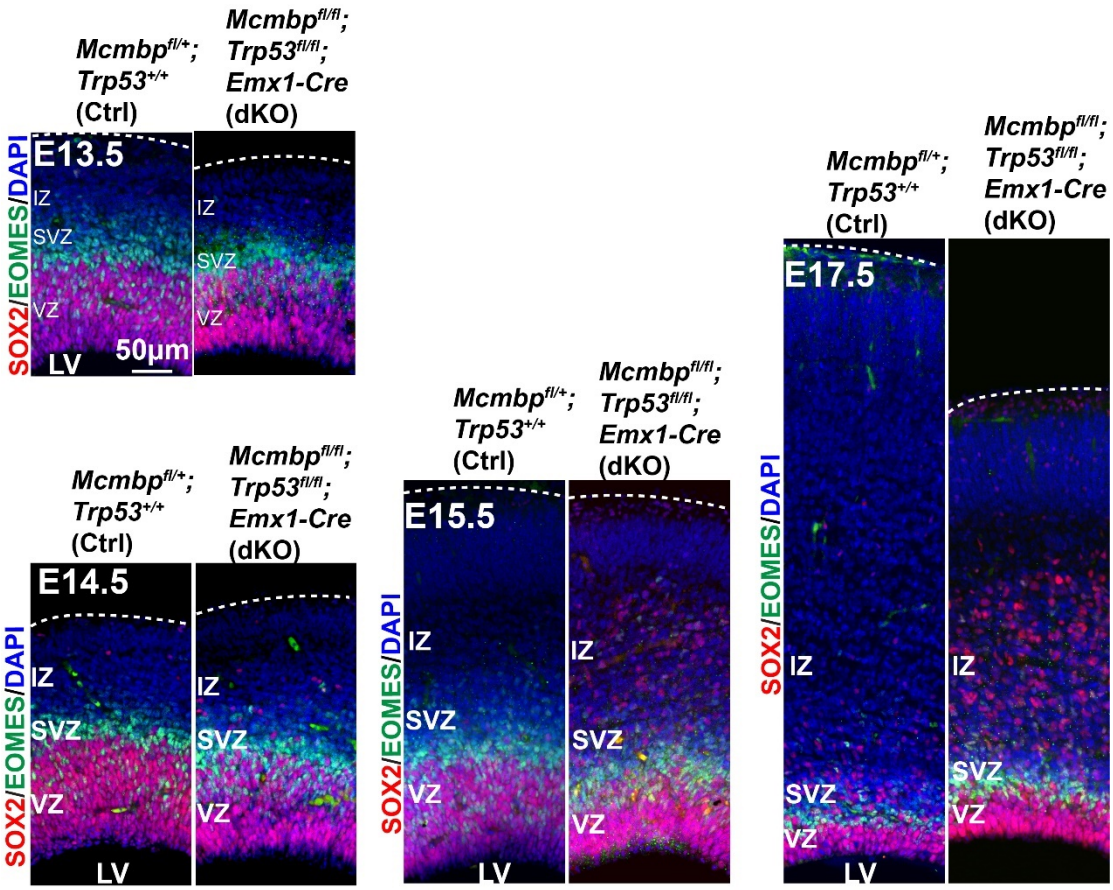

Figure S4. Representative images of RGCs SOX2+ and IPCs EOMES+ at E13.5, E14.5, E15.5 and E17.5 dKO cortex respectively. Related to Figure 4.

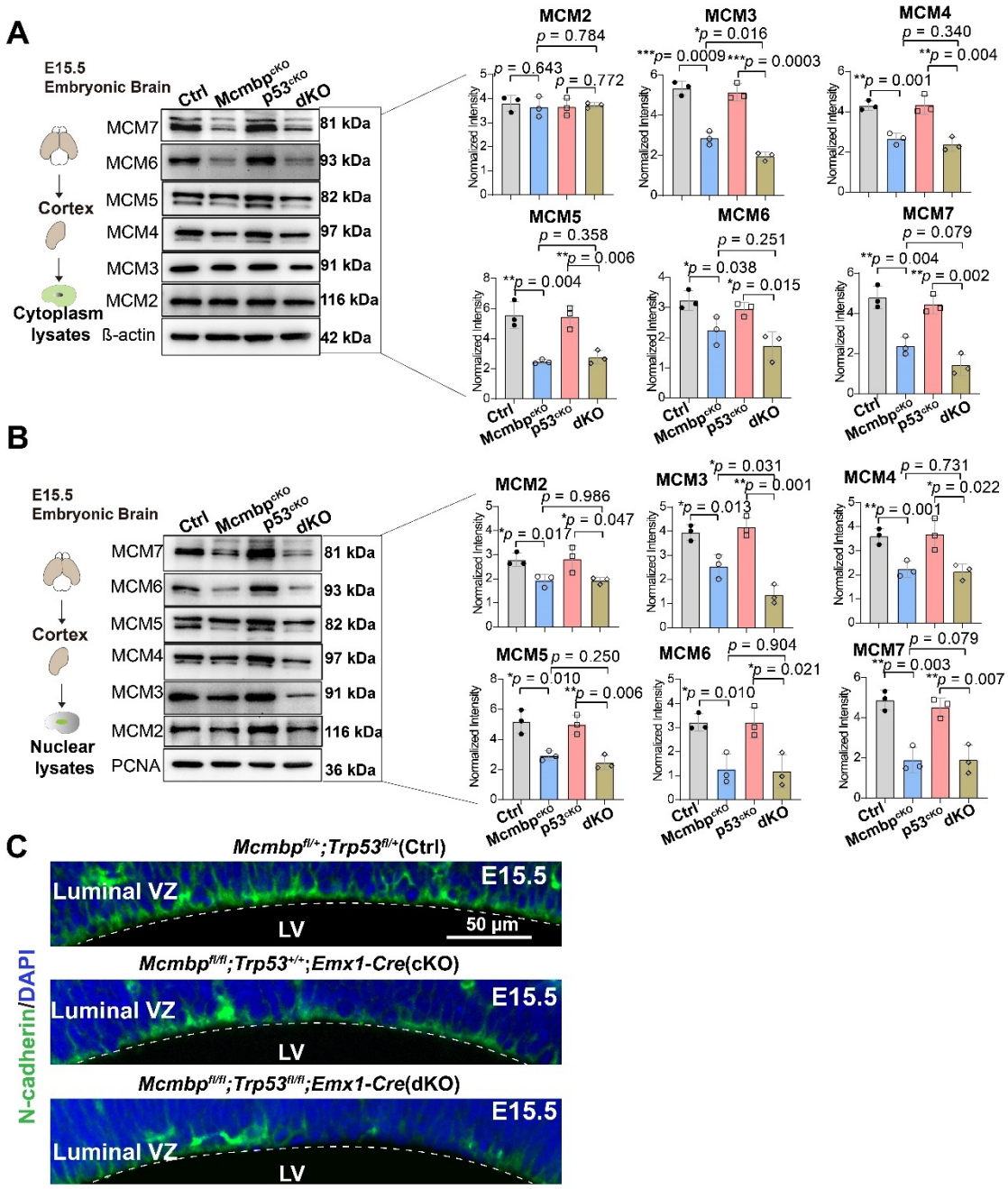

Figure S5. MCM complex subunits expression and cell adhesion analysis in *Mcmbp/Trp53* dKO. Related to Figure 6.

(A-B) Western blotting on cytoplasm (A) and nuclear lysates (B), and quantitative analysis identifying MCM3 as the only MCM subunit significantly repressed in dKO.

(C) Representative images of adhension marker N-cadherin+ at E15.5 dKO cortex.

References

Anders, S., and Huber, W. (2010). Differential expression analysis for sequence count data. Genome Biol *11*, R106.

Anders, S., Pyl, P.T., and Huber, W. (2015). HTSeq--a Python framework to work with high-throughput sequencing data. Bioinformatics *31*, 166-169.

Bettencourt-Dias, M., and Glover, D.M. (2007). Centrosome biogenesis and function: centrosomics brings new understanding. Nat Rev Mol Cell Biol *8*, 451-463.

Brosh, R., Sarig, R., Natan, E.B., Molchadsky, A., Madar, S., Bornstein, C., Buganim, Y., Shapira, T., Goldfinger, N., Paus, R.*, et al.* (2010). p53-dependent transcriptional regulation of EDA2R and its involvement in chemotherapy-induced hair loss. FEBS Lett *584*, 2473-2477.

Bulchand, S., Grove, E.A., Porter, F.D., and Tole, S. (2001). LIM-homeodomain gene Lhx2 regulates the formation of the cortical hem. Mech Dev *100*, 165-175.

Chen, J., Bardes, E.E., Aronow, B.J., and Jegga, A.G. (2009). ToppGene Suite for gene list enrichment analysis and candidate gene prioritization. Nucleic Acids Res *37*, W305-311.

Dehay, C., Kennedy, H., and Kosik, K.S. (2015). The outer subventricular zone and primate-specific cortical complexification. Neuron *85*, 683-694.

Di Marco, B., Crouch, E.E., Shah, B., Duman, C., Paredes, M.F., de Almodovar, C.R., Huang, E.J., and Alfonso, J. (2020). Reciprocal Interaction between Vascular Filopodia and Neural Stem Cells Shapes Neurogenesis in the Ventral Telencephalon. Cell Reports *33*.

Fernández, V., Llinares-Benadero, C., and Borrell, V. (2016). Cerebral cortex expansion and folding: what have we learned? Embo J *35*, 1021-1044.

Fietz, S.A., Kelava, I., Vogt, J., Wilsch-Brauninger, M., Stenzel, D., Fish, J.L., Corbeil, D., Riehn, A., Distler, W., Nitsch, R.*, et al.* (2010). OSVZ progenitors of human and ferret neocortex are epithelial-like and expand by integrin signaling. Nat Neurosci *13*, 690-699.

Fitsiori, A., Nguyen, D., Karentzos, A., Delavelle, J., and Vargas, M.I. (2011). The corpus callosum: white matter or terra incognita. Br J Radiol *84*, 5-18.

Forsburg, S.L. (2004). Eukaryotic MCM proteins: beyond replication initiation. Microbiol Mol Biol Rev *68*, 109-131.

Fragkos, M., Ganier, O., Coulombe, P., and Mechali, M. (2015). DNA replication origin activation in space and time. Nat Rev Mol Cell Biol *16*, 360-374.

Ghosh, S., Vassilev, A.P., Zhang, J., Zhao, Y., and DePamphilis, M.L. (2011). Assembly of the human origin recognition complex occurs through independent nuclear localization of its components. J Biol Chem *286*, 23831-23841.

Goodarzi, A.A., Noon, A.T., Deckbar, D., Ziv, Y., Shiloh, Y., Lobrich, M., and Jeggo, P.A. (2008). ATM signaling facilitates repair of DNA double-strand breaks associated with heterochromatin. Mol Cell *31*, 167-177.

Gorski, J.A., Talley, T., Qiu, M., Puelles, L., Rubenstein, J.L., and Jones, K.R. (2002). Cortical excitatory neurons and glia, but not GABAergic neurons, are produced in the Emx1-expressing lineage. J Neurosci *22*, 6309-6314.

Gotz, M., and Huttner, W.B. (2005). The cell biology of neurogenesis. Nat Rev Mol Cell Biol *6*, 777-788.

Gruber, R., Zhou, Z., Sukchev, M., Joerss, T., Frappart, P.O., and Wang, Z.Q. (2011). MCPH1 regulates the neuroprogenitor division mode by coupling the centrosomal cycle with mitotic entry through the Chk1-Cdc25 pathway. Nat Cell Biol *13*, 1325-1334.
Hansen, D.V., Lui, J.H., Parker, P.R., and Kriegstein, A.R. (2010). Neurogenic radial glia in the outer subventricular zone of human neocortex. Nature *464*, 554-561.
Hevner, R.F., Shi, L., Justice, N., Hsueh, Y., Sheng, M., Smiga, S., Bulfone, A., Goffinet, A.M., Campagnoni, A.T., and Rubenstein, J.L. (2001). Tbr1 regulates differentiation of the preplate and layer 6. Neuron *29*, 353-366.
Higginbotham, H., Guo, J., Yokota, Y., Umberger, N.L., Su, C.Y., Li, J., Verma, N., Hirt, J., Ghukasyan, V., Caspary, T.*, et al.* (2013). Arl13b-regulated cilia activities are essential for polarized radial glial scaffold formation. Nat Neurosci *16*, 1000-1007.
Huang, K., Han, Y., Chen, K., Pan, H., Zhao, G., Yi, W., Li, X., Liu, S., Wei, P., and Wang, L. (2021). A hierarchical 3D-motion learning framework for animal spontaneous behavior mapping. Nat Commun *12*, 2784.
Insolera, R., Bazzi, H., Shao, W., Anderson, K.V., and Shi, S.H. (2014). Cortical neurogenesis in the absence of centrioles. Nat Neurosci *17*, 1528-1535.
Kaas, J.H. (2019). The origin and evolution of neocortex: From early mammals to modern humans. Prog Brain Res *250*, 61-81.
Kalogeropoulou, A., Lygerou, Z., and Taraviras, S. (2019). Cortical Development and Brain Malformations: Insights From the Differential Regulation of Early Events of DNA Replication. Front Cell Dev Biol *7*, 29.
Karakatsani, A., Shah, B., and de Almodovar, C.R. (2019). Blood Vessels as Regulators of Neural Stem Cell Properties. Front Mol Neurosci *12*.
Keil, J.M., Doyle, D.Z., Qalieh, A., Lam, M.M., Funk, O.H., Qalieh, Y., Shi, L., Mohan, N., Sorel, A., and Kwan, K.Y. (2020). Symmetric neural progenitor divisions require chromatin-mediated homologous recombination DNA repair by Ino80. Nat Commun *11*, 3839.
Klusmann, I., Rodewald, S., Muller, L., Friedrich, M., Wienken, M., Li, Y., Schulz-Heddergott, R., and Dobbelstein, M. (2016). p53 Activity Results in DNA Replication Fork Processivity. Cell Rep *17*, 1845-1857.
Knockleby, J., and Lee, H. (2010). Same partners, different dance: involvement of DNA replication proteins in centrosome regulation. Cell Cycle *9*, 4487-4491.
Kraeuter, A.K., Guest, P.C., and Sarnyai, Z. (2019). The Open Field Test for Measuring Locomotor Activity and Anxiety-Like Behavior. Methods Mol Biol *1916*, 99-103.
Kuipers, M.A., Stasevich, T.J., Sasaki, T., Wilson, K.A., Hazelwood, K.L., McNally, J.G., Davidson, M.W., and Gilbert, D.M. (2011). Highly stable loading of Mcm proteins onto chromatin in living cells requires replication to unload. J Cell Biol *192*, 29-41.
Kwan, K.Y., Sestan, N., and Anton, E.S. (2012). Transcriptional co-regulation of neuronal migration and laminar identity in the neocortex. Development *139*, 1535-1546.
Lee, Y., Katyal, S., Downing, S.M., Zhao, J., Russell, H.R., and McKinnon, P.J. (2012). Neurogenesis requires TopBP1 to prevent catastrophic replicative DNA damage in early progenitors. Nat Neurosci *15*, 819-826.
Lindström, M.S., Bartek, J., and Maya-Mendoza, A. (2022). p53 at the crossroad of DNA replication and ribosome biogenesis stress pathways. Cell Death Differ *29*, 972-982.

Loo, L., Simon, J.M., Xing, L., McCoy, E.S., Niehaus, J.K., Guo, J., Anton, E.S., and Zylka, M.J. (2019). Single-cell transcriptomic analysis of mouse neocortical development. Nat Commun *10*, 134.
Lui, J.H., Hansen, D.V., and Kriegstein, A.R. (2011). Development and evolution of the human neocortex. Cell *146*, 18-36.
Martin, M. (2011). Cutadapt Removes Adapter Sequences from High-Throughput Sequencing Reads. EMBnet Journal *17*, 10-12.
McEvilly, R.J., de Diaz, M.O., Schonemann, M.D., Hooshmand, F., and Rosenfeld, M.G. (2002). Transcriptional regulation of cortical neuron migration by POU domain factors. Science *295*, 1528-1532.
McKinnon, P.J. (2013). Maintaining genome stability in the nervous system. Nat Neurosci *16*, 1523-1529.
McKinnon, P.J. (2017). Genome integrity and disease prevention in the nervous system. Genes Dev *31*, 1180-1194.
Miyamoto, Y., Sakane, F., and Hashimoto, K. (2015). N-cadherin-based adherens junction regulates the maintenance, proliferation, and differentiation of neural progenitor cells during development. Cell Adh Migr *9*, 183-192.
Monuki, E.S., Porter, F.D., and Walsh, C.A. (2001). Patterning of the dorsal telencephalon and cerebral cortex by a roof plate-Lhx2 pathway. Neuron *32*, 591-604.
Mora-Bermudez, F., Taverna, E., and Huttner, W.B. (2022). From stem and progenitor cells to neurons in the developing neocortex: key differences among hominids. Febs J *289*, 1524-1535.
Morimoto, K., Tabata, H., Takahashi, R., and Nakajima, K. (2024). Interactions between neural cells and blood vessels in central nervous system development. Bioessays *46*.
Nakatani, T., Lin, J., Ji, F., Ettinger, A., Pontabry, J., Tokoro, M., Altamirano-Pacheco, L., Fiorentino, J., Mahammadov, E., Hatano, Y.*, et al.* (2022). DNA replication fork speed underlies cell fate changes and promotes reprogramming. Nat Genet *54*, 318-327.
Nieminuszczy, J., Schwab, R.A., and Niedzwiedz, W. (2016). The DNA fibre technique – tracking helicases at work. Methods *108*, 92-98.
Nishiyama, A., Frappier, L., and Méchali, M. (2011). MCM-BP regulates unloading of the MCM2-7 helicase in late S phase. Gene Dev *25*, 165-175.
Pertea, M., Kim, D., Pertea, G.M., Leek, J.T., and Salzberg, S.L. (2016). Transcript-level expression analysis of RNA-seq experiments with HISAT, StringTie and Ballgown. Nat Protoc *11*, 1650-1667.
Saito, Y., Santosa, V., Ishiguro, K.I., and Kanemaki, M.T. (2022). MCMBP promotes the assembly of the MCM2-7 hetero-hexamer to ensure robust DNA replication in human cells. Elife *11*.
Sedlackova, H., Rask, M.B., Gupta, R., Choudhary, C., Somyajit, K., and Lukas, J. (2020). Equilibrium between nascent and parental MCM proteins protects replicating genomes. Nature *587*, 297-+.
Shen, Q., Wang, Y., Dimos, J.T., Fasano, C.A., Phoenix, T.N., Lemischka, I.R., Ivanova, N.B., Stifani, S., Morrisey, E.E., and Temple, S. (2006). The timing of cortical neurogenesis is encoded within lineages of individual progenitor cells. Nature Neuroscience *9*, 743-751.

Shi, L., Qalieh, A., Lam, M.M., Keil, J.M., and Kwan, K.Y. (2019). Robust elimination of genome-damaged cells safeguards against brain somatic aneuploidy following Knl1 deletion. Nat Commun *10*, 2588.

Sousa, A.M.M., Meyer, K.A., Santpere, G., Gulden, F.O., and Sestan, N. (2017). Evolution of the Human Nervous System Function, Structure, and Development. Cell *170*, 226-247.

Steinbaugh, M., Pantano, L., Kirchner, R., Barrera, V., Chapman, B., Piper, M., Mistry, M., Khetani, R., Rutherford, K., Hofmann, O.*, et al.* (2018). bcbioRNASeq: R package for bcbio RNA-seq analysis [version 2; peer review: 1 approved, 1 approved with reservations]. F1000Research *6*.

Stuermer, A., Hoehn, K., Faul, T., Auth, T., Brand, N., Kneissl, M., Putter, V., and Grummt, F. (2007). Mouse pre-replicative complex proteins colocalise and interact with the centrosome. Eur J Cell Biol *86*, 37-50.

Telley, L., Agirman, G., Prados, J., Amberg, N., Fièvre, S., Oberst, P., Bartolini, G., Vitali, I., Cadilhac, C., Hippenmeyer, S.*, et al.* (2019). Temporal patterning of apical progenitors and their daughter neurons in the developing neocortex. Science *364*, 547-+.

Thomsen, E.R., Mich, J.K., Yao, Z., Hodge, R.D., Doyle, A.M., Jang, S., Shehata, S.I., Nelson, A.M., Shapovalova, N.V., Levi, B.P.*, et al.* (2016). Fixed single-cell transcriptomic characterization of human radial glial diversity. Nat Methods *13*, 87-93.

Thornton, G.K., and Woods, C.G. (2009). Primary microcephaly: do all roads lead to Rome? Trends Genet *25*, 501-510.

Trapnell, C., Hendrickson, D.G., Sauvageau, M., Goff, L., Rinn, J.L., and Pachter, L. (2013). Differential analysis of gene regulation at transcript resolution with RNA-seq. Nature Biotechnology *31*, 46-+.

Tronche, F., Kellendonk, C., Kretz, O., Gass, P., Anlag, K., Orban, P.C., Bock, R., Klein, R., and Schutz, G. (1999). Disruption of the glucocorticoid receptor gene in the nervous system results in reduced anxiety. Nat Genet *23*, 99-103.

Walchli, T., Mateos, J.M., Weinman, O., Babic, D., Regli, L., Hoerstrup, S.P., Gerhardt, H., Schwab, M.E., and Vogel, J. (2015). Quantitative assessment of angiogenesis, perfused blood vessels and endothelial tip cells in the postnatal mouse brain. Nat Protoc *10*, 53-74.

Yadav, A.K., and Polasek-Sedlackova, H. (2024). Quantity and quality of minichromosome maintenance protein complexes couple replication licensing to genome integrity. Commun Biol *7*, 167.

Yan, H., Merchant, A.M., and Tye, B.K. (1993). Cell cycle-regulated nuclear localization of MCM2 and MCM3, which are required for the initiation of DNA synthesis at chromosomal replication origins in yeast. Genes Dev *7*, 2149-2160.

Zhang, W., Yang, S.-L., Yang, M., Herrlinger, S., Shao, Q., Collar, J.L., Fierro, E., Shi, Y., Liu, A., Lu, H.*, et al.* (2019). Modeling microcephaly with cerebral organoids reveals a WDR62–CEP170–KIF2A pathway promoting cilium disassembly in neural progenitors. Nature Communications *10*.